THESIS FOR THE DEGREE OF LICENTIATE OF ENGINEERING

Membrane Filtration of Wood Components

Investigation of Fouling Layer Characteristics using Fluid Dynamic Gauging

KENNETH G. ARANDIA

Department of Chemistry and Chemical Engineering
CHALMERS UNIVERSITY OF TECHNOLOGY
Gothenburg, Sweden 2022

Membrane Filtration of Wood Components
Investigation of Fouling Layer Characteristics using Fluid Dynamic Gauging

KENNETH G. ARANDIA

Technical Report No. 2022:01

Department of Chemistry and Chemical Engineering
Chalmers University of Technology
SE-412 96 Gothenburg
Sweden
Phone: +46 (0)31 772 1000

Cover: Lagom by Angel Lee
Printed by Chalmers Reproservice
Gothenburg, Sweden 2022

Membrane Filtration of Wood Components

Investigation of Fouling Layer Characteristics using Fluid Dynamic Gauging

KENNETH G. ARANDIA

Department of Chemistry and Chemical Engineering
Chalmers University of Technology

Abstract

As process industries transition from using fossil-based to bio-based resources, energy-efficient and highly selective operations will be required to process lignocellulosic biomass. Membrane separation, as a highly efficient operation, can be employed in the fractionation and dewatering of streams containing lignocellulosic biomass. The application of membrane separation in these processes has nevertheless proved to be challenging due to membrane fouling: the process by which suspended or dissolved substances are deposited on the surface or within the pores of a membrane. An in-depth mechanistic understanding of such membrane fouling behavior is therefore necessary in order to devise appropriate strategies to address fouling.

In this work, the *in situ* monitoring technique fluid dynamic gauging (FDG), was used to investigate the fouling behavior of two feed streams containing wood components: a liquor obtained when wood was treated using steam explosion (STEX) and a microcrystalline cellulose (MCC) suspension. The cross-flow ultrafiltration (UF) of STEX liquors was performed at 200 kPa transmembrane pressure (TMP) using 10 kDa polysulfone membranes, whereas the cross-flow microfiltration (MF) of MCC suspensions was operated at 40 kPa TMP using 0.45 μm polyethersulfone membranes.

Experimental results show that FDG provides valuable information regarding membrane fouling in both cross-flow MF and UF. The FDG profiles obtained during the STEX liquor fouling experiments revealed that an initial thick fouling layer of high resistance was formed rapidly. After this initial phase, the resistance increased further but only gradually, which may be due to pore blocking and/or rearrangement of the structure of the fouling layer. These results also indicate that the highest resistance of the fouling layer is close to the membrane. In the MCC fouling experiments, highly resilient layers were formed close to the membrane surface, as supported by the presence of attractive energy regions at the close interparticle separations identified via molecular dynamics (MD) simulations. These results highlight how FDG, when complemented with MD simulations, can provide a better mechanistic understanding of the fouling behavior of streams containing wood components during cross-flow filtration.

Keywords: fluid dynamic gauging, membrane fouling, cross-flow filtration, wood components, steam explosion, microcrystalline cellulose

ᜉᜇᜌᜓᜈ᜔

PADAYON

(adv.) keep going, carry on

List of Publications and Presentations

This thesis is based on the following appended papers:

I. **Development of a fluid dynamic gauging method for the characterization of fouling behavior during cross-flow filtration of a wood extraction liquor**
Kenneth Arandia, Upasna Balyan & Tuve Mattsson
Food and Bioproducts Processing, **2021**, 128, 30–40.

II. **Fouling characteristics of microcrystalline cellulose during cross-flow microfiltration: Insights gained from fluid dynamic gauging and molecular dynamics simulations**
Kenneth Arandia, Nabin Kumar Karna, Tuve Mattsson, Anette Larsson & Hans Theliander
Manuscript

Part of this work has been presented at the following conferences:

Investigation of membrane fouling using fluid dynamic gauging during cross-flow filtration of wood extracts
Kenneth Arandia, Upasna Balyan & Tuve Mattsson
12th International Congress on Membranes and Membrane Processes (ICOM 2020)
Oral presentation
Presented by: Tuve Mattsson
Online: Live and On-demand (London, United Kingdom), December 7–11, 2020

***In situ* investigation of cake fouling using fluid dynamic gauging during cross-flow microfiltration of an organic model material**
Kenneth Arandia, Nabin Kumar Karna, Anette Larsson & Hans Theliander
Euromembrane 2021
Oral presentation
Copenhagen, Denmark, November 29 – December 2, 2021

Contribution Report

The author of this thesis has made the following contributions to the publications included:

I. First author. Planned and performed the majority of the experimental work. Analyzed and interpreted the results in collaboration with the co-authors. Wrote the original draft of the manuscript. Reviewed and edited the article with support from Tuve Mattsson.

II. Co-first author. Planned and performed all experimental work. Nabin Kumar Karna was responsible for the molecular dynamics simulations. Analyzed and interpreted fluid dynamic gauging results. Wrote, reviewed and edited the manuscript together with Nabin Kumar Karna, with support from Hans Theliander and Anette Larsson.

Abbreviations and Symbols

Abbreviations

ASL	Acid-soluble lignin
COM	Center of mass
CFD	Computational fluid dynamics
CFV	Cross-flow velocity [$\mathrm{m\,s^{-1}}$]
FDG	Fluid dynamic gauging
LVDT	Linear variable differential transformer
MD	Molecular dynamics
MF	Microfiltration
NF	Nanofiltration
MCC	Microcrystalline cellulose
MWCO	Molecular weight cut-off
PES	Polyethersulfone
PMF	Potential of mean force
PSU	Polysulfone
RO	Reverse osmosis
SEM	Scanning electron microscopy
STEX	Steam explosion
TMP	Transmembrane pressure [Pa]
UF	Ultrafiltration
US	Umbrella sampling

Symbols

D_x	Size below which x% of all particles are found
d	Inner diameter of the gauge tube [m]
d_t	Inner diameter of the nozzle orifice [m]
dp	Pressure drop over the FDG probe [mbar]
h	Gauge height above the fouling layer [m]
h_0	Gauge height above the membrane [m]
J	Flux [$\mathrm{L\,m^{-2}\,h^{-1}}$]
m_g	Gauging mass flow rate [$\mathrm{kg\,s^{-1}}$]
r	Interparticle separation [m]
R_{m+c}	Total resistance (membrane and cake) [$\mathrm{m^2\,L^{-1}}$]
Re_{duct}	Duct flow Reynolds number [–]
ΔG	Free energy [$\mathrm{J\,mol^{-1}\,m^{-2}}$]
ΔH	Enthalpic contribution to the free energy [$\mathrm{J\,mol^{-1}\,m^{-2}}$]
δ	Fouling layer thickness [m]
μ	Dynamic viscosity of the fluid [Pa s]
Π	Osmotic pressure [Pa]
ρ	Density of the fluid [$\mathrm{kg\,m^{-3}}$]
$\tau_{w,max}$	Fluid shear stress [Pa]
$T\Delta S$	Entropic contribution to the free energy [$\mathrm{J\,mol^{-1}\,m^{-2}}$]

Contents

1 | Introduction

The main driving force in developing sustainable technologies, the climate crisis, implies the need to shift away from using fossil-based materials towards renewable, bio-based resources. This paradigm shift necessitates current process industries being transformed into advanced and novel biorefineries that can process lignocellulosic biomass, such as forest and agricultural residues, and thereby create more viable options for the world's increasing energy and material requirements. By recovering valuable components from underutilized process streams, lignocellulosic biorefineries have an immense potential for contributing to a bio-based economy through the conversion of lignocellulosic biomass feedstocks into renewable, value-added products [1], thus promoting their sustainable production and consumption.

The chemical and mechanical processes necessary for the production of novel materials sourced from lignocellulosic feedstocks must not only be simple, scalable and selective but also have a high material yield and energy efficiency, coupled with minimal waste production. These processes will involve various unit operations and require reactors, separation equipment and the suchlike. One highly efficient operation that will be needed in the fractionation step, and in some cases, pre-dewatering of process streams containing lignocellulosic biomass, is membrane separation. Membrane separation can be an attractive prospect since these processes offer energy-efficient and selective pathways for recovering valuable components and can, moreover, be operated continuously at low to moderate temperatures. The modular design of membrane separation simplifies their scale-up as well as the expansion of the production capacity of an existing unit [2]. These advantages of membrane separation can be beneficial to the development of lignocellulosic biorefineries.

1.1 Membrane Filtration in Lignocellulosic Biorefineries

The field of membrane technology has thrived over the last few decades with applications in various industrial sectors, e.g. food processing, pharmaceutical technology, drinking water production and wastewater treatment. Membrane filtration can be expected to be employed in the pre-treatment and downstream processing of lignocellulosic biomass [2,3] in future biorefineries. As an energy-efficient and highly selective operation, pressure-driven membrane filtration can recover valuable components from process streams by fractionation, concentration and purification.

Studies on membrane filtration of lignocellulosic biomass have continually gained significant interest [4-6] as industries are developing to transition towards the sustainable processing of lignocellulosic materials. However, for lignocellulosic biomass to be utilized efficiently, the operational costs of membrane separation must be minimized because separation accounts for a substantial proportion of the total manufacturing costs.

The application of membrane filtration in lignocellulosic biorefineries has proved to be challenging, primarily due to membrane fouling [7,8]. Fouling impairs separation performance due to the deposition of suspended or dissolved substances on the surface, at the pore openings or within the pores of a membrane [9] and leads either to a decline in the flow rate at a constant transmembrane pressure (TMP) or an increase in the TMP required to achieve a constant flow rate. Fouling-related performance losses entail additional operational costs due to downtime and membrane cleaning. Further investments in a larger membrane unit (e.g. two parallel units) may be necessary to sustain a continuous operation. Although fouling occurs, more or less, in all processes where membrane separation is applied, it is practically inevitable in complex, heterogeneous systems involving lignocellulosic components and measures are therefore essential in controlling its effects. There have been significant developments in the investigation and characterization of membrane fouling, however, studies on the mechanistic understanding of fouling behavior remain limited; in-depth knowledge of fouling phenomena is therefore paramount for devising appropriate fouling strategies.

1.2 Aim and Objectives

This thesis aims at gaining in-depth knowledge of membrane fouling during cross-flow filtration of wood components. The main focus is placed on the following objectives:

1) To develop the fluid dynamic gauging (FDG) technique for the *in situ* and real-time monitoring of fouling layer characteristics.

2) To investigate the underlying mechanisms of membrane fouling, using FDG measurements and molecular dynamics (MD) simulations.

3) To devise appropriate strategies for improving the performance of membrane separation.

The content of this thesis is based on two studies: the first paper covers the development of a method using FDG to investigate the fouling behavior and shifts in fouling modes during the cross-flow ultrafiltration (UF) of steam explosion (STEX) liquors on polysulfone (PSU) membranes, while the second paper focuses on the mechanistic understanding of the fouling behavior of a model material, i.e. microcrystalline cellulose (MCC), on polyethersulfone (PES) membranes during cross-flow microfiltration (MF) using FDG and MD simulations. These studies, which are appended, are referred to hereafter as Papers I and II, respectively.

1.3 Wallenberg Wood Science Center

This work has been a part of the Wallenberg Wood Science Center (WWSC), a joint research center for The Royal Institute of Technology (KTH), Chalmers University of Technology and Linköping University. The main focus of WWSC is to create new materials from trees by building knowledge and competence for future innovative value creation from forest-based raw materials. The studies presented in this thesis are part of the WWSC project entitled "Fractionation of wood components using membrane filtration," which focuses on facilitating the energy-efficient recovery and fractionation of extracted wood components using membrane separation processes.

2 | Membrane Separation

Membrane filtration employs a selectively permeable membrane that separates a process stream into two fractions: the retentate and permeate. The stream that passes through the membrane is called the permeate, while the more concentrated stream that flows across the membrane is called the retentate. The properties of the membrane determine which components can pass through the membrane and end up on the permeate side. Membrane filtration is a more energy-efficient alternative to conventional thermal separation processes, such as distillation and evaporation, because of its lower energy input and selectivity that can be fine-tuned to isolate the components desired [10].

2.1 Membrane Materials

Membranes can be manufactured synthetically from porous polymers, ceramics, metals or liquids [11]. Synthetic membranes are employed in industrial membrane operations and can be categorized according to the material used: the two main types are polymeric (organic) and ceramic (inorganic) membranes. Depending on their morphology, these can have either a homogeneous or heterogeneous structure and either a symmetric (isotropic) or asymmetric (anisotropic) design based on the pore structure.

Organic polymeric membranes are made from materials with different wetting properties. In general, hydrophilic membranes (e.g. cellulose acetate, regenerated cellulose and polyamide) can achieve higher water flux and are less adsorptive than hydrophobic membranes (e.g. PSU, PES and polypropylene), making them more resistant to fouling [11]. However, the chemical and thermal stabilities of hydrophilic membranes are inferior compared to hydrophobic membranes. In industrial operations, hydrophobic membranes are more commonly used and are typically coated with a hydrophilic layer to improve their wetting properties. This improvement in hydrophilicity is crucial as robust membranes are required in the food and beverage industry, where stringent sterilization procedures are implemented.

Ceramic membranes are made from inorganic materials (e.g. alumina, titania and zirconia) and are renowned for their excellent thermal resistance, chemical stability and high mechanical strength. Compared to polymeric membranes, ceramic membranes have better reliability and longer lifespan but are, on the other hand, very brittle and considerably more expensive [12]. Although using ceramic membranes incurs higher initial capital costs than polymeric membranes, it will, in many cases, prove to be beneficial in the long term since they are more durable and can withstand several years of operation.

2.2 Pressure-driven Membrane Filtration

The primary driving force for flow through a membrane is the TMP, i.e. the applied differential pressure that pushes a liquid through a membrane. Pressure-driven membrane-based separation processes can be classified into four categories: MF, UF, nanofiltration (NF) and reverse osmosis (RO). These processes are specified based on their pore size and are typically described in terms of molecular weight cut-off (MWCO) for UF, NF and RO. MWCO is the molecular weight of a solute that corresponds to a 90% rejection coefficient [9]. Fig. 2.1 shows the typical pore size range, operating pressures and examples of rejected species for each membrane process. The operating pressure increases with decreasing pore size, with MF membranes having the most open pores and being operated at the lowest TMP.

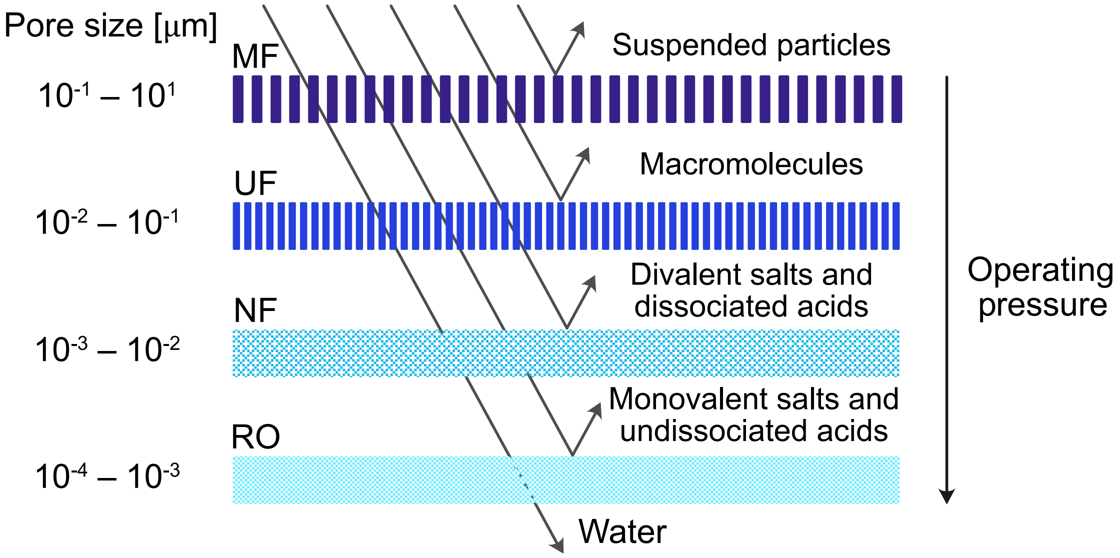

Fig. 2.1. Typical process conditions and rejection behavior of pressure-driven membrane filtration processes.

Cross-flow filtration

Cross-flow membrane filtration has been developed from dead-end filtration, in which a filter cake is formed while fluid passes through a permeable separation device. In cross-flow filtration, the feed flows parallel to the membrane surface, as shown in Fig. 2.2, ideally forming a thin, dynamic concentration layer rather than a thick,

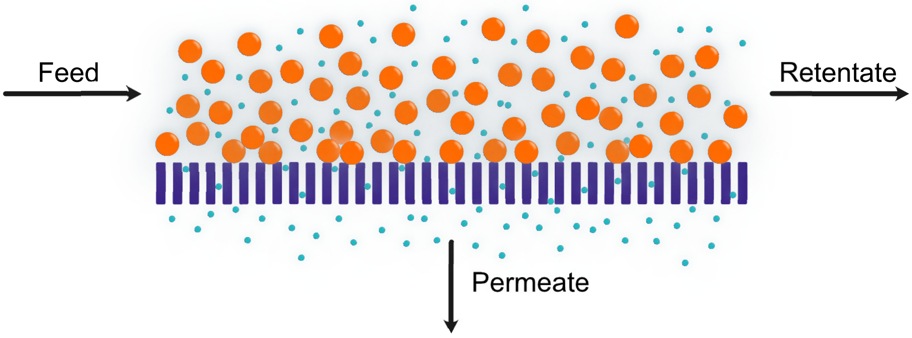

Fig. 2.2. A cross-flow filtration system illustrating the feed, permeate and retentate streams.

stationary filter cake, as a result of shear forces that re-suspend some of the rejected materials. The configuration in cross-flow filtration systems varies depending on the concentration required of the desired product stream, which can be either the permeate or the retentate, or both.

The flux, J, is defined as the permeate flow, Q_p divided by the total membrane surface area, A_m, and is typically expressed in liters per square meters of membrane surface area per hour ($\mathrm{L\,m^{-2}\,h^{-1}}$) thus:

$$J = \frac{Q_p}{A_m} \tag{2.1}$$

In pressure-driven membrane filtration, the TMP is defined as the average of the pressures on the feed side, p_f, and on the retentate side, p_r, minus the pressure on the permeate side, p_p:

$$\mathrm{TMP} = \frac{p_f + p_r}{2} - p_p \tag{2.2}$$

Concentration polarization

A concentration gradient at the boundary layer is formed when solutes or suspended particles are moved towards the membrane surface by permeate flow. This phenomenon is called concentration polarization, by which solutes are retained and accumulate at the membrane surface [12]. It is illustrated in Fig. 2.3, where the solute or particle concentration is higher near the membrane surface, generating resistance to flux [11].

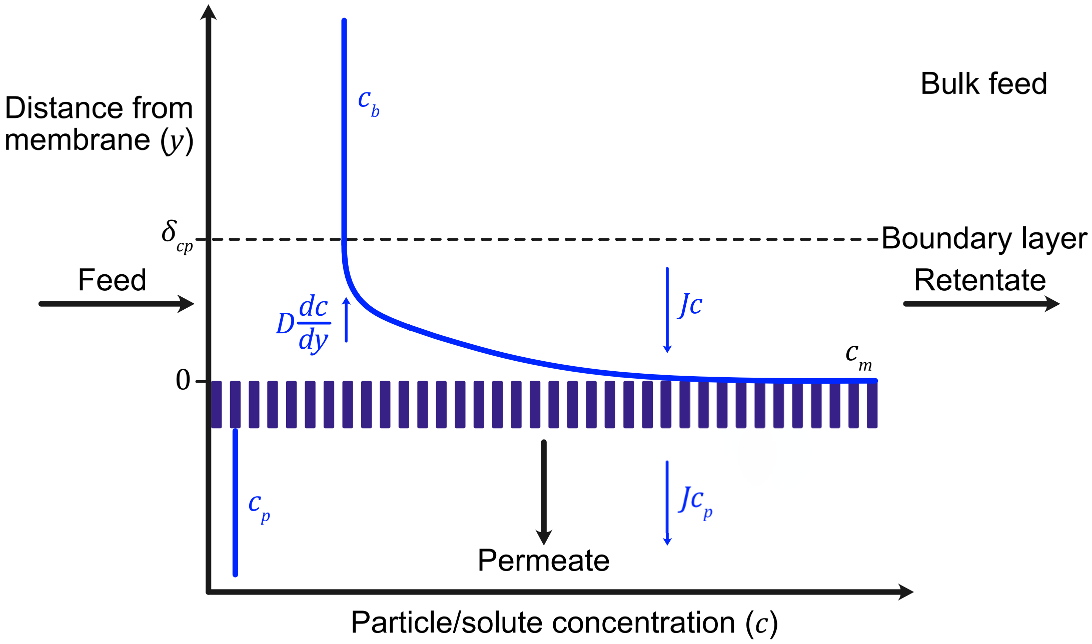

Fig. 2.3. Schematic diagram of a concentration profile caused by concentration polarization under steady state conditions.

Concentration polarization always occurs and is most significant for molecules or dissolved salts (i.e. for UF, NF or RO) as these are highly influenced by convective forces and diffusion. In MF, heterogeneous mixtures containing dissolved macromolecules and small particles may decrease the effect of concentration polarization since they influence the conditions at the boundary layer. A steady-state condition is reached when a balance between the convective flow of solutes or particles towards the membrane is counteracted by the back-transport [13] into the bulk feed due to diffusion and/or turbulence. The following equation describes the concentration profile with respect to distance from the membrane:

$$Jc + D_{CP}\frac{dc}{dy} = Jc_p \tag{2.3}$$

where c is the concentration of the particle or solute, D_{CP} is the apparent diffusion coefficient, y is the distance from the membrane, and c_p is the concentration of the permeate.

Eq. 2.3 can be simplified by integrating the entire function with bounds from the membrane surface, $y = 0$, to the concentration polarization boundary layer distance, δ_{CP}:

$$\frac{c_m - c_p}{c_b - c_p} = exp\left(\frac{J\delta_{CP}}{D_{CP}}\right) = exp\left(\frac{J}{k_{CP}}\right) \tag{2.4}$$

where c_m is the concentration at the membrane, c_b is the concentration in the bulk liquid and k_{CP} is the mass transfer coefficient associated with concentration polarization (which is D_{CP} divided by δ_{CP}).

Rearranging Eq. 2.4, the flux can be expressed as:

$$J = k_{CP}\ln\left(\frac{c_m - c_p}{c_b - c_p}\right) \tag{2.5}$$

2.3 Membrane Fouling

Fouling is the deposition of dissolved or suspended substances on the surface of a membrane, at its pore openings or within its pores [9]. It limits the production capacity of the operation by lowering the permeation rate or changing the membrane's selectivity over time [11]. Fouling can be classified based on the location of the foulants with respect to the membrane material. Reversible fouling can be removed effectively by physical cleaning since foulants are attached loosely to the membrane surface and result in the formation of a cake or gel layer, or concentration polarization. Irreversible fouling, on the other hand, can only be removed by chemical cleaning because foulants are bound tightly to the membrane due to adsorption or pore blocking. The different types of fouling in membrane filtration are presented in Fig. 2.4.

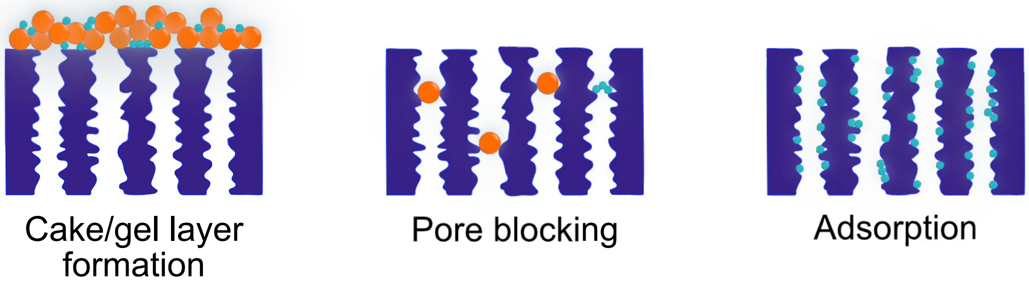

Fig. 2.4. Schematic representation of the different types of membrane fouling.

2.4 Flux Models

There are different mechanistic models for determining the fouling rate during cross-flow filtration; in this section, only models related to flux are presented.

In a pure solvent system, Darcy's law states that J is proportional to the TMP, as given in Eq. 2.6:

$$J = \frac{\text{TMP}}{\mu}\frac{k_m}{\delta_m} \tag{2.6}$$

where μ is the dynamic viscosity of the fluid, k_m is the permeability of the membrane and δ_m is its thickness.

The TMP is the only driving force of the separation process and the membrane resistance, R_m, is the only resistance that acts against it. Eq. 2.6 can be simplified by substituting the permeability and thickness terms, k_m and δ_m, with R_m:

$$J = \frac{\text{TMP}}{\mu R_m} \tag{2.7}$$

where R_m is δ_m divided by k_m.

R_m can be determined by simply filtering a pure solvent (e.g. water) and taking into account the porosity and pore size distribution of the membrane.

When filtering a solution or a suspension, the osmotic pressure, Π, generally works against flux when the concentration of the dissolved species on the feed side is significantly higher than that on the permeate side. The resistance term in Eq. 2.7 can be extended to include the resistance due to reversible and irreversible fouling aside from the membrane resistance. These resistance terms can be added in series to give the resistance-in-series model shown in Eq. 2.8:

$$J = \frac{\text{TMP} - \Pi}{\mu R_T} = \frac{\text{TMP} - \Pi}{\mu(R_m + R_{rev} + R_{irrev})} \tag{2.8}$$

where the total resistance, R_T, is the sum of R_m, the reversible fouling resistance R_{rev} and the irreversible fouling resistance, R_{irrev}.

The resistance-in-series model in Eq. 2.8 can be expanded to include the different types of reversible and irreversible fouling:

$$J = \frac{\mathrm{TMP} - \Pi}{\mu(R_m + R_c + R_{CP} + R_p)} \tag{2.9}$$

where R_c, R_{CP}, and R_p are cake, concentration polarization and pore fouling resistances, respectively.

Models describing blocking mechanisms

The calculation of the permeate flux from the resistance-in-series model in Eq. 2.8 does not indicate whether the flux decline is caused by cake filtration, pore fouling or indeed both. One way to identify which type of fouling occurs is by autopsy or *ex situ* analysis of the fouled membrane [14].

Hermia developed a methodology for identifying different types of blocking mechanisms for dead-end filtration at constant pressure [15]. This model is based on the following empirical equation:

$$\frac{d^2t}{dV^2} = k\left(\frac{dt}{dV}\right)^n \tag{2.10}$$

where *V* is the filtrate volume, *t* is the filtration time and the variable constants *k* and *n* are based on the type of fouling, as summarized in Table 2.1. Fig. 2.5 depicts the different types of blocking mechanisms, where the assumption is a uniform cylindrical pore distribution across the membrane surface.

Table 2.1. Blocking mechanisms used for modelling membrane fouling phenomena and their respective constants [15].

Mechanism	*k*	*n*
Cake filtration	$\frac{\varphi_c c_b \mu}{A_m^2 TMP}$	0
Intermediate blocking	$\frac{\sigma}{A_m}$	1
Standard blocking	$\frac{2\phi_{ads}}{\delta_m} A_m^{-0.5} J_0^{0.5}$	1.5
Complete blocking	$J_0\sigma$	2

φ_c is the specific cake resistance [m kg^{-1}], σ is blocked membrane surface area per unit volume of permeate, ϕ_{ads} is the volume of particles retained by pores per unit volume of permeate and J_0 is the initial flux.

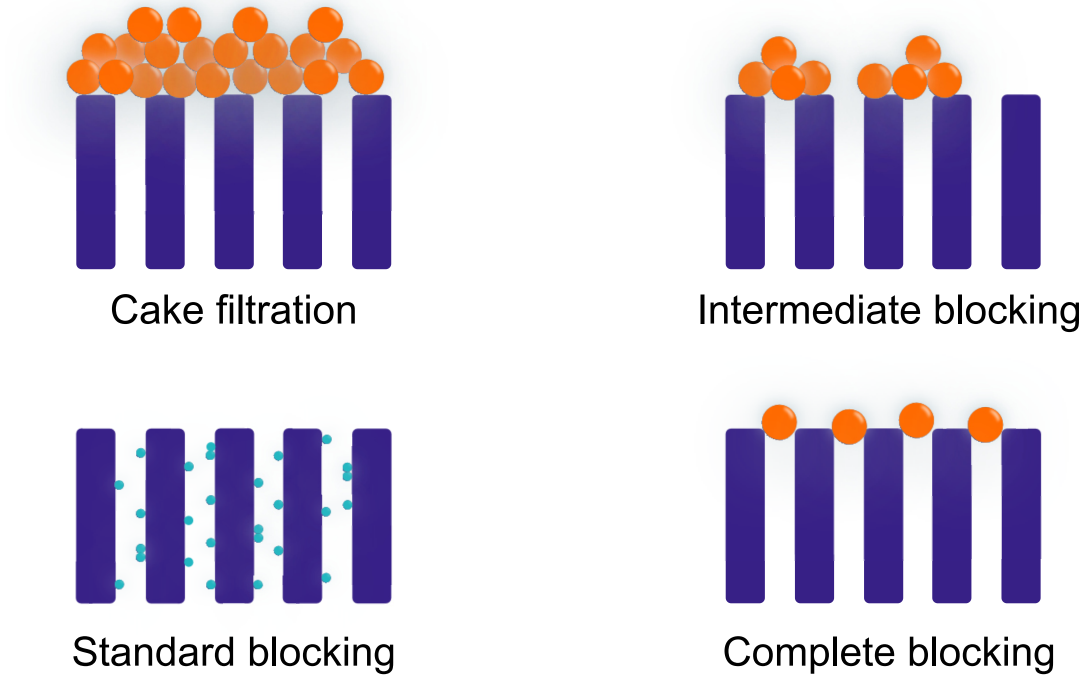

Fig. 2.5. Blocking and cake filtration mechanisms as described by Hermia [15].

Cake filtration occurs when particles larger than the pore opening are deposited on the membrane surface. It is presumed that the cake resistance, R_c, is directly proportional to the total filtrate volume. In Hermia's model, the right hand term in Eq. 2.10 becomes constant for cake filtration ($n = 0$):

$$\frac{d^2t}{dV^2} = k\left(\frac{dt}{dV}\right)^0 = constant \tag{2.11}$$

The term "standard blocking" has been coined to describe internal pore fouling due to the adsorption of particles on the pore walls. The decline in pore volume is proportional to the total filtrate volume, as particles smaller than the pore opening are adsorbed onto the pore walls. Complete blocking is when a single particle blocks a pore completely upon reaching the surface of the membrane, thereby reducing its available surface area. Intermediate blocking is a more realistic mechanism for surface fouling than complete blocking: whilst a particle may block an open pore, it can also settle on top of another particle. Some pores remain unblocked while particles are deposited on top of each other and hence a slower flux decline is observed than for complete blocking. Whilst the blocking mechanisms mentioned above are relevant for particles, charge and geometric considerations must, however, be taken into account when molecules or ions are present. Non-spherical particles may have a greater contact area with the membrane than spherical particles and changes in the ionic strength could affect the formation of a cake layer (e.g. an increase in ionic strength could decrease the local and average filtration resistances [16].

Hermia's methodology is applicable primarily to dead-end filtration and at the early stages of cross-flow filtration [17]. As the methods for determining the fouling rate for cross-flow filtration are more complex than dead-end filtration, the back-transport of solutes or particles into the bulk flow must be taken into account.

Critical flux model

Field *et al.* introduced the critical flux model, which states that no observable fouling will take place below a critical permeate flux, J_{crit}, during cross-flow filtration [18]. Plotting the permeate flux as a function of TMP, as seen in Fig. 2.6, shows that the flux is directly proportional to the TMP for pure solvent systems. The flux of a feed material containing solutes and particles increases steadily at low TMPs; it tapers off after passing the critical flux and eventually stops increasing upon reaching the limiting flux. The limiting flux is influenced greatly by the type of membrane fouling that occurs. Its value may be raised by increasing the temperature of the system, increasing the shear forces or reducing the solute or particle concentration in the feed material.

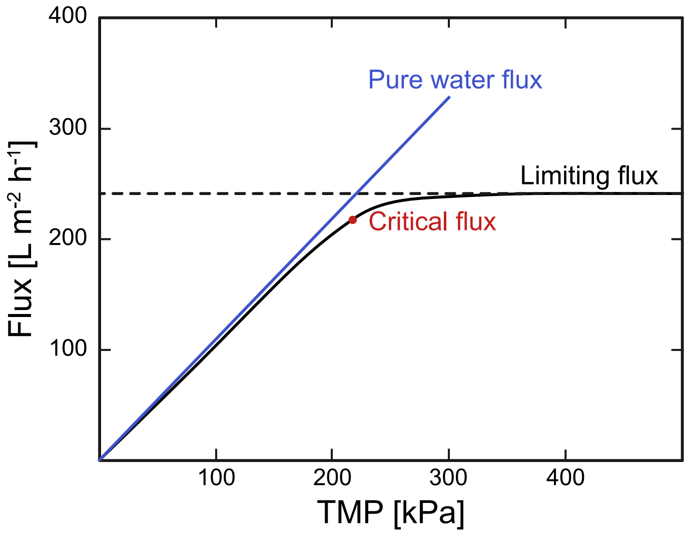

Fig. 2.6. Permeate flux curves showing the critical and limiting flux.

2.5 Membrane Cleaning

Careful selection and optimization of process conditions such as TMP, cross-flow velocity (CFV) and/or temperature ensure that the effects of fouling are minimized;

membranes can also be functionalized or pre-treated to improve productivity. Fouling occurs nevertheless, and mitigation strategies and periodic cleaning measures are implemented in industrial membrane operations to ensure continuous operation and maintain performance.

There are two types of methods available for cleaning membranes: physical and chemical. As stated in the previous section, reversible fouling can be removed effectively by physical cleaning, whereas irreversible fouling can only be removed by chemical cleaning. Physical cleaning methods include forward flushing, backflushing, backpulsing, sponge ball and ultrasonic cleaning [19]. Forward flushing involves applying feed water or permeate forward at an elevated CFV: the rapid flow and resulting turbulence releases the foulants deposited on the membrane surface. Backflushing is a reversed filtration process whereby the permeate is forced through the membrane from the permeate side to the feed or retentate side to remove particles that have accumulated on the membrane, and particularly those adsorbed onto its pores. Backpulsing is another kind of reverse flow cleaning that induces a periodic TMP reversal for a short duration to dislodge foulants deposited on the surface of the membrane or in its pores. Sponge ball cleaning involves balls made of polyurethane or other material being inserted into the membrane module for a short duration of time to scrub foulants from the membrane surface. Ultrasonic cleaning employs ultrasonic waves whereby convective currents increase turbulence and provide vigorous mixing. The physical effects of the implosive collapse of cavitation bubbles aid in generating micromixing in a liquid, thereby enhancing the cleaning process.

Chemical cleaning may be applied when physical cleaning has been unable to restore the flux or membrane selectivity. The membrane is flushed with an acidic, alkaline or enzymatic cleaning agent that typically contains surface-active agents to solubilize or break down foulants on a membrane [20]. The system can also be operated at an elevated CFV and temperature to improve cleaning. The composition and concentration of the cleaning agent and the duration of the cleaning process are dependent on the foulants and the type of fouling. Alkaline cleaning agents are normally based on sodium hydroxide (NaOH) and/or sodium hypochlorite (NaOCl), which are usually applied to remove organic foulants. In contrast, acidic cleaning agents are often based on hydrochloric acid (HCl), phosphoric acid (H_3PO_4), or sulfuric acid (H_2SO_4), which are applied to remove scaling from inorganic compounds. In general, acidic and alkaline cleaning reduces the membrane's lifespan due to the aggressive nature of the chemicals: milder approaches, such as enzymatic cleaning

[21], are therefore preferred whenever possible. Enzymes can be formulated to target specific foulants but they are, however, are more expensive than acidic and alkaline cleaning agents.

The economic implications of membrane cleaning must be taken into consideration. Membrane cleaning measures require downtime and productivity will therefore be reduced. Fouling will also reduce productivity: not only will the production rate be lowered but also energy costs may be raised due to an increased TMP. For a specific filtration system, a mechanistic understanding of membrane fouling and cleaning is crucial in order to carefully assess the membrane material, operating conditions and cleaning measures that are necessary to mitigate or manage the effects of fouling. A cost-benefit analysis of cleaning a membrane versus its replacement is also beneficial in saving time, money and resources; moreover, the possibility of fine-tuning the design of membrane operations will result in optimized productivity.

2.6 Membrane Separation of Wood Components

Different wood components can be considered as potential foulants in the membrane separation of process streams from lignocellulosic biorefineries. These process streams may contain the following wood components: cellulose, hemicelluloses, lignin, extractives, proteins and inorganic compounds. Moreover, they may have a wide range of particle sizes and molecular weights and their concentration may vary, depending on the wood species used and the chemical processes involved. Among all these potential foulants, it is only the three main constituents of wood, namely cellulose, hemicellulose and lignin, that will be described in more detail below.

Cellulose

Cellulose is a linear and unbranched polymer comprised of repeating D-glucopyranose units linked together by a β-(1$\rightarrow$4)-glycosidic bond, as shown in Fig. 2.7. As the most abundant polymer in nature, cellulose is found primarily in the cell walls of plants together with hemicelluloses and lignin, and accounts for 40-45% of the dry substance in most pulpwood species [22]. The strong inter and intramolecular hydrogen bonding between the hydroxyl groups contributes to the stiffness of the chain. These bonds result in the cellulose chains aggregating to form microfibrils, which have both a highly ordered crystalline region and a less ordered amorphous region.

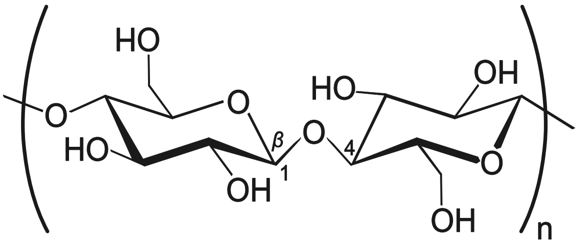

Fig. 2.7. A cellobiose unit showing the β-(1→4)-glycosidic bond.

Microcrystalline cellulose (MCC) is a partially depolymerized cellulose prepared by mild acid hydrolysis, where the crystallites are released due to the hydrolysis of highly reactive amorphous regions. MCC is commonly used as a stabilizer, thickener, emulsifier and binding agent in cosmetics and personal care products and in the food and beverage and pharmaceutical industries. Several MCC filtration studies have been conducted to determine its local filtration properties: Mattsson *et al.* observed the formation of compressible filter cakes during the dead-end filtration of MCC suspensions [23,24], while Zhou *et al.* investigated the effects of pH and cross-flow regime on the fouling characteristics of MCC during cross-flow MF [25,26].

Hemicellulose

Hemicelluloses are linear or branched heteropolymers of much shorter length than cellulose, i.e. they have a lower degree of polymerization. In contrast to cellulose, which has a crystalline structure, hemicelluloses have a random and amorphous structure that can be easily hydrolyzed by acids into their monomeric components of D-glucose, D-galactose, D-mannose, D-xylose and L-arabinose. Xylans are the most common hemicelluloses present in hardwoods, while glucomannans are predominant in softwoods.

In the Kraft pulping process, hemicelluloses typically end up in the recovery boiler for energy generation despite their relatively low heating value [27]. This means that it is potentially more beneficial to recover hemicelluloses and utilize them in the production of bio-based materials. Studies on the recovery of hemicelluloses using MF and/or UF have been carried out on process waters from thermomechanical pulp mills [28,29], spent sulfite liquors [30] and wheat bran using heat pretreatment [31]. Although these studies were successful in isolating and purifying hemicelluloses, the decline in performance due to membrane fouling remains to be addressed.

Lignin

Lignin is an amorphous, heterogeneous polymer with randomly cross-linked phenylpropane units. It makes the cell wall hydrophobic and provides stiffness by fixating cellulose and hemicellulose in a rigid matrix. It also serves as a barrier against microbial and environmental degradation. The β-O-4 linkage in lignin is the most important chemical bond between its phenylpropane units, also known as monolignols. The three main monolignols present in lignin are *p*-coumaryl alcohol, sinapyl alcohol and coniferyl alcohol (Fig. 2.8).

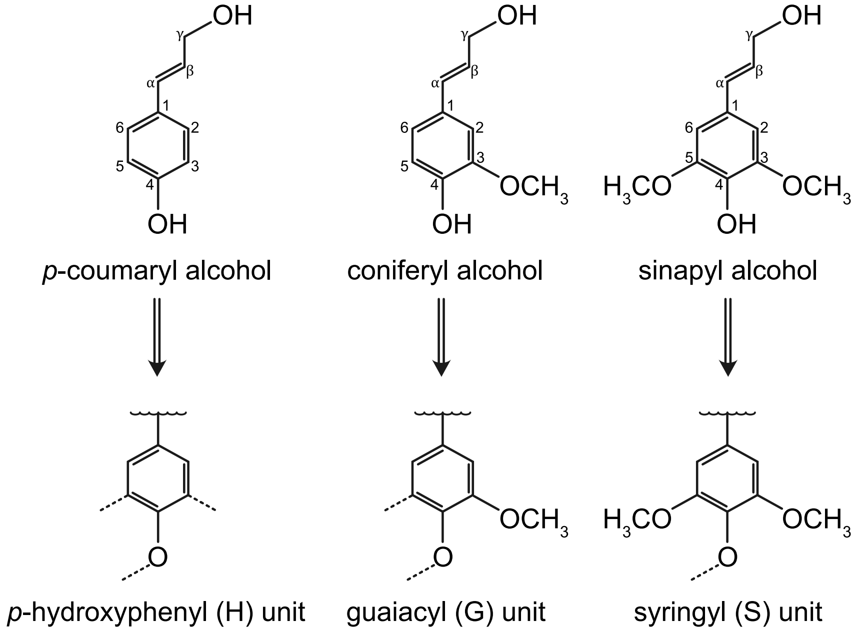

Fig. 2.8. The three main monolignols found in lignin and their respective lignin structural units.

The structure and composition of lignin are highly dependent on the type of wood used. Softwoods have an HG-type of lignin, with more guaiacyl (G) units and trace amounts of *p*-hydroxyphenyl (H) units, thus making coniferyl alcohols the predominant building block in softwood lignin (90-95% of total lignin source). In contrast, hardwoods have a GS-type of lignin comprised of different proportions of guaiacyl (G) and syringyl (S) units, with sinapyl alcohol being 50-75% of the total lignin source.

Kraft lignin, an industrial lignin obtained from Kraft pulp, has been investigated for its fouling behavior by Mattsson *et al.* [32,33]. They found that a 10-fold increase in the fluid shear stress was required to remove fouling layers formed closer to the membrane than those formed on the surface of the cake [32]. At different TMPs, the thickness of the cake layers formed increases with increasing TMP [33].

3 | Fluid Dynamic Gauging

Membrane fouling behavior is typically characterized in terms of decline in permeate flux or increase in TMP. These parameters do not, however, provide direct and reliable measures of the thickness, composition and type of membrane fouling. Advanced techniques that employ *in situ* and real-time monitoring of the development of fouling layers are therefore necessary to provide hydrodynamic information of both the fouling behavior and the properties of the layers formed.

Numerous *in situ* techniques have been developed over the years to investigate the formation of fouling layers: these include direct observation [34], laser-based techniques [35], confocal laser scanning microscopy [36], ultrasonic time domain reflectometry [37], nuclear magnetic resonance imaging [38], small angle x-ray scattering [39], electrical impedance spectroscopy [40] and fluid dynamic gauging (FDG) [41]. These techniques differ in their operating principles, measurement capabilities, limitations and potential applications [42]; careful assessment of their cost, operability, accuracy and versatility [43] is therefore important when selecting the most suitable technique.

Among the available *in situ* techniques mentioned above for monitoring membrane fouling, FDG offers unique information that other techniques cannot attain. This real-time monitoring technique provides an indication of the thickness and strength properties of fouling layers. FDG is a relatively inexpensive technique applicable for different types of fluids and involves minimal sample preparation: it is an ideal way of making measurements in industrial membrane operations since it can be fully automated. This technique was first developed by Tuladhar *et al.* for measuring the local thickness of soft deposits on solid surfaces [41]. Since then, FDG has been developed extensively for monitoring fouling behavior during membrane filtration [44,45].

3.1 Theory and Principles

The governing principle behind FDG is based on fluid mechanics, whereby a pressure drop is generated due to flow constriction between the tip of a nozzle and the surface of a fouling layer when fluid is withdrawn through the probe, as illustrated in Fig. 3.1. The pressure drop over the FDG probe, *dp*, is measured by taking arbitrary points in the surrounding liquid region and down the length of the gauge tube away from the

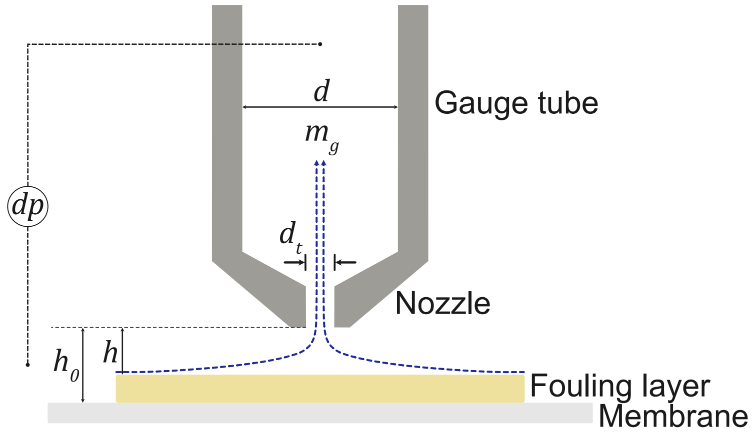

Fig. 3.1. Schematic diagram of the FDG probe over a fouled membrane surface. The probe consists of a gauge tube with a tapered nozzle, where *d* is the inner diameter of the gauge tube (d = 3 mm) and d_t is the inner diameter of the nozzle orifice (d_t = 0.5 mm). m_g is the gauging mass flow rate, *dp* is the pressure drop over the probe, h_0 is the gauge height above the membrane and *h* is the gauge height above the fouling layer.

nozzle opening. As the probe approaches the surface of the fouling layer, the fouling layer thickness, δ, is estimated using the *dp* values a known position of the membrane.

The fouling layer thickness, δ, is given by Eq. 3.1:

$$\delta = h_0 - h \tag{3.1}$$

where *h* is the gauge height above the fouling layer and h_0 is the gauge height above the membrane.

An example of experimental data for the response recorded during FDG measurements of a pristine (unfouled) membrane and a fouled membrane is shown in Fig. 3.2. The non-linear wall response for the pristine membrane can be divided into two zones: asymptotic ($h/d_t >$ 0.25) and incremental ($h/d_t \leq$ 0.25). In the former zone, low and relatively constant *dp* values are measured, while a sharp increase in *dp* values is observed as h/d_t decreases in the latter zone. When FDG thickness measurements are conducted on a fouled membrane, the difference in h/d_t values of the fouled membrane and the pristine membrane represents the thickness of the fouling layers formed, where a larger difference corresponds to a thicker fouling layer.

The cohesive and adhesive strength of fouling layers formed can be estimated simultaneously with FDG thickness measurements. As the probe is moved closer

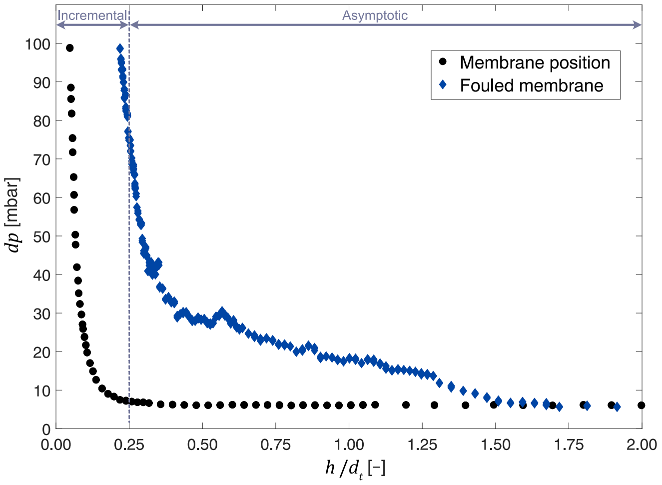

Fig. 3.2. An example of experimental *dp* vs. h/d_t data of the position of a pristine membrane and the response of a fouled membrane. $h/d_t = 0.25$ marks the boundary between the incremental and asymptotic zones of the pristine membrane.

to the surface of a fouling layer, fluid shear stress is exerted on the surface by the probe, which allows the shear-induced removal of fouling layers to be tracked. The maximum shear stress, $\tau_{w,max}$, can be estimated using Eq. 3.2, with the assumption of a creeping concentric flow between parallel plates:

$$\tau_{w,max} = \frac{6\mu m_g}{\pi \rho h^2} \cdot \frac{1}{d_t} \tag{3.2}$$

where μ is the dynamic viscosity of the fluid, m_g is the gauging mass flow rate, ρ is the density of the fluid, h is the gauge height above the fouling layer and d_t is the inner diameter of the nozzle orifice.

$\tau_{w,max}$ provides an indication of the shear stress required to shear off individual cake layers, thereby allowing the local cohesive or adhesive strength of the cake to be estimated. $\tau_{w,max}$ is in the region directly underneath the inner edge of the nozzle rim at a radial distance $d_t/2$ from the central axis of the gauge tube.

3.2 Modes of Operation

There are two modes of operation for conducting FDG measurements: the mass flow and the pressure mode. The main difference between them is the parameter that is kept constant: either the differential pressure, *dp*, or the gauging flow rate, m_g.

Mass flow mode

In mass flow mode, m_g is regulated in order to keep *dp* constant when the thickness of a fouling layer is estimated by lowering the probe towards the fouled layer. This mode is the original configuration when Tuladhar *et al.* developed the technique [41]. However, filtration systems in mass flow mode cannot be operated at higher pressures since the flow is discharged at ambient conditions. In addition, it is difficult to control the rate at which the gauge fluid is withdrawn while maintaining a constant pressure head.

Pressure mode

The pressure mode involves *dp* being regulated in order to keep m_g constant when the probe is lowered towards the fouling layer. This is the preferred mode for fouling studies in flowing environments: significantly higher pressures can be applied and the overall flow conditions are preserved due to the controlled rate of fluid withdrawal [46]. The studies presented in this thesis employed pressure-mode FDG, where the thickness estimations are made by measuring *dp* while fluid is being withdrawn through the probe at a constant m_g.

3.3 Previous FDG Studies

Quasi-static FDG

Tuladhar *et al.* initially developed FDG to investigate the fouling behavior of soft films of butter, adhesive foam-based tape and deposits of whey protein on a stainless-steel plate [41]. Their experimental tests were carried out in a quasi-static system, where the fouled surface is placed in a vessel filled with a liquid that has no bulk movement and the gauge fluid is withdrawn by means of a siphon effect.

Quasi-static FDG studies were also conducted by Chew *et al.* on non-Newtonian fluids using a test rig with an FDG probe that can be moved along an axis parallel to the surface, where a fixed hydrostatic head induces fluid flow into the probe that is positioned normal to the surface of interest [47]. Chew *et al.* confirmed the possibility of tracking the shear-induced removal of tomato paste from a stainless-steel substrate by generating shear as fluid is withdrawn through the probe [48]. In further studies, quasi-static systems were investigated for solvent-based cleaning of polymeric fouling [49] and biofilm adhesion on different surfaces [50].

Scanning mode FDG is an adaptation to *quasi-static* systems that allows different areas of a fouled surface to be analyzed by moving the probe along x and y-axes [51]. This FDG configuration was used to study enzyme-based cleaning of gelatin films and egg yolk [52]. Another adaptation to *quasi-static* systems was made by Yang *et al.*, who studied the adhesion of petroleum jelly to a stainless-steel surface using zero discharge FDG (pressure-mode) [53].

A combination of experimental methods and computational fluid dynamics (CFD) was employed in predicting shear stress distributions [47,48] and selecting an appropriate nozzle design from different nozzle geometries for a particular application [54,55].

Duct flow FDG

Further studies conducted by Tuladhar *et al.* simulated whey protein fouling in heat exchangers by using a heat transfer module with an attached FDG probe. They worked in a duct flow environment, where a plate assembly separates liquids flowing in ducts with a square cross-section. The FDG gauge was operated in mass flow mode and a heat flux sensor was incorporated to monitor the thermal resistance of the fouling layer [56,57]. Inorganic scaling of stainless-steel plates [58] and protein fouling [59] were also investigated in duct flow environments. Gu *et al.*, who demonstrated the first use of pressure-mode FDG, performed CFD simulations for duct flow systems and found good agreement between the predicted and experimental data [60]. Further FDG studies were conducted for applications to annular flow sections in heat exchangers [61,62].

Membrane FDG

FDG was expanded further to membrane fouling studies for measuring the thickness of model materials. Chew *et al.* investigated particle fouling during dead-end filtration of glass ballotini suspensions [44]. Jones *et al.* were the first to perform FDG studies during cross-flow MF (mass-flow mode) of sugar beet molasses using PSU membranes at high CFV under turbulent conditions [63,64]. In contrast, Lister *et al.* used a duct flow FDG, operated under laminar flow conditions, to perform cross-flow membrane filtration (pressure-mode FDG) of spherical glass beads [65].

Other membrane FDG studies have also investigated model materials such as yeast suspensions [66], synthetic microparticles [67], Kraft lignin [32,33] and MCC [25,26], which demonstrate the versatility of this technique for different kinds of foulants. In more recent FDG studies, Tsia *et al.* developed the sideways fluid dynamic gauging concept to track *in situ* and in real-time the changes in the thickness of soft solid layers whose properties change significantly on contact with liquid [68,69]. They also incorporated an inductive proximity sensor, placed in a convergent FDG nozzle, to determine the distance between the tip of the nozzle and the fouling layer formed from a metallic substrate [70]. These membrane studies have applied FDG successfully to membranes and porous surfaces in a flowing environment. However, a more detailed understanding of the fouling mechanisms is necessary.

In the membrane FDG studies presented in this thesis, pressure-mode FDG was employed to investigate the fouling behavior of lignocellulosic feed materials on flat sheet polymeric membranes: STEX liquors on PSU membranes in Paper I and MCC suspensions on PES membranes in Paper II.

4 | Materials and Methods

4.1 Raw Materials

Polymeric membranes

Flat sheet polymeric membranes of different pore sizes were used in the two studies: a 10 kDa PSU membrane and a 0.45 μm PES membrane in Papers I and II, respectively. A permanently hydrophilic PSU membrane (UFX10 pHt^{TM}, Alfa Laval), with a pure water flux of 412–466 L m^{-2} h^{-1} at 400 kPa TMP, was used in the cross-flow UF experiments in Paper I. This membrane has an asymmetric configuration, with a thin PSU skin layer placed above a non-woven, polypropylene support layer. In Paper II, a hydrophilic PES membrane (Supor®, Pall Corporation), with a pure water flux of $3.5 \cdot 10^4$ L m^{-2} h^{-1} at 70 kPa TMP, was mounted for the cross-flow MF experiments. Both PSU and PES membranes were cut to dimensions of 200 mm x 30 mm (L × W) to fit into a cross-flow filtration cell with an active membrane surface area of $2.4 \cdot 10^{-3}$ m^2 (150 mm × 16 mm).

Softwood chips

Industrially-cut softwood chips sourced from a pulp mill in the southern part of Sweden were used as the raw material for the cross-flow UF experiments in Paper I. The wood chips were comprised of ∼75% Norway spruce (*Picea abies*) and ∼25% pine (*Pinus sylvestris*), which were dried at ambient temperature and pressure.

Microcrystalline cellulose

Commercially-available MCC (Avicel® PH-105, FMC Biopolymers) was selected as the model material for the cross-flow MF experiments in Paper II. The nominal particle size of MCC was specified by the manufacturer to be 20 μm.

4.2 Feed Preparation

Steam explosion liquor

Prior to being subjected to a mild steam explosion (STEX) process, the wood chips were sorted manually, which included the removal of bark and knobs, to achieve a more uniform size distribution. The smallest wood chip had dimensions of about 17 mm × 20 mm × 2 mm (L × W × H), while the largest was about 60 mm × 45 mm × 6 mm. An amount of 500 g (dry basis) of sorted wood chips was immersed in deionized water in a closed vessel, and then impregnated by applying vacuum for 5 min, followed by applying 500 kPa of nitrogen gas for a further 5 min. The chips were left under pressure for 2–3 h and the water was drained before being placed in the STEX reactor.

The STEX equipment used, and its operating procedures, have been described by Jedvert et al. [71]. The STEX treatment conditions were kept mild to limit degradation of the wood components caused by acid hydrolysis [72]. The STEX operation was performed using saturated steam at 700 kPa ($\sim$165 °C) for 20 min to extract a hemicellulose-rich fraction, i.e. the feed material for the cross-flow UF. This STEX liquor was separated from the steam-exploded wood chips by filtering through a Büchner funnel with a plastic grid mesh ($<$ 1 mm openings). 1.5–2 L of STEX liquor were collected for every 500 g of wood chips processed and for each cross-flow UF experiment, two batches of STEX liquors were mixed. The STEX liquors were then cooled to room temperature and stored at 5 °C before the cross-flow UF experiments were undertaken.

Microcrystalline cellulose suspension

A dilute suspension with a solids content of 0.15 vol% was prepared by suspending 9.80 g of MCC in 4 L deionized water. Measurements made on the same batch of MCC showed that its specific surface area and solid density were 2.1 $\mathrm{m^2\,g^{-1}}$ and 1560 $\mathrm{kg\,m^{-3}}$, respectively [73]. Prior to each cross-flow filtration experiment, the MCC particles were subjected to mechanical pretreatment by homogenizing the dilute suspension in a 5 L baffled feed tank using an IKA Ultra-Turrax® T50 with an S50 N-G45F dispersing element at a rotational speed of 10 000 rpm for 15 min. Consistent swelling of the particles was ensured by stirring the suspension constantly for a minimum of 12 h, using a pitched two-blade impeller, at an ambient temperature of 22-23 °C and at its unadjusted pH of 6.2. For each cycle of cross-flow MF, the mechanically-pretreated suspension was diluted further to a concentration of 0.02 vol% and four 5 L suspensions were prepared for each MF sequence.

4.3 Cross-flow Filtration Rig

A bench-scale, stainless-steel cross-flow filtration test rig was used in all cross-flow filtration experiments: Fig. 4.1 shows the test rig equipped with a flow cell and an FDG probe. The flow cell has a rectangular channel with dimensions of 150 mm × 16 mm ×

15 mm. The FDG probe is a gauge tube with a tapered nozzle; the inner diameter of the tube, d, is 3 mm and the inner diameter of the nozzle orifice, d_t, is 0.5 mm. The location of the probe was fixed at the center of the flow channel and its vertical movement was controlled by a stepper motor attached to a linear guide rail (NanotecST4209S1006-B); its minimum linear movement is 0.31 μm. The membrane was mounted at the bottom of the flow cell with two supporting layers placed underneath to secure its position. A porous polypropylene sheet was positioned directly underneath the membrane which, in turn, was supported by a perforated stainless steel slab with holes 2 mm in diameter.

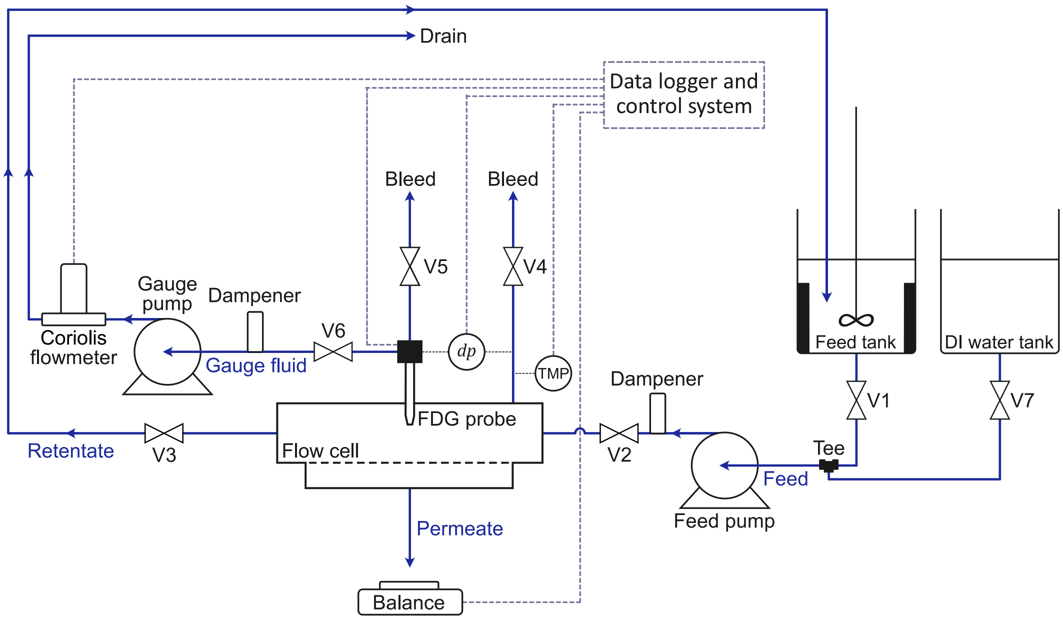

Fig. 4.1. Schematic diagram of the modified cross-flow filtration test rig showing the different process streams: feed, permeate, retentate and gauge fluid.

Technical specifications

The test rig was operated in a feed-and-bleed configuration, whereby the feed material was circulated through the test section by the feed pump (GB-P35.PVS.A.B1, Ismatec) at a constant CFV and the retentate was recycled back to the inlet of the feed tank. The feed material was placed in a 5 L baffled feed tank stirred at ~300 rpm by a pitched two-blade impeller. The TMP was regulated by the needle valve V3. A precision balance (Quintix®3102-1S, Sartorius) was placed below the flow cell to collect the permeate at atmospheric pressure. The gauging mass flow rate during FDG measurements was maintained by the gauge pump (DBS.11EEET2NMM104, Tuthill). A 3-way tee union, a 12 mm ball valve (V7) and a separate tank for deionized water were introduced in Paper II to simplify the changing procedure of the feed material and to prevent air bubbles from entering into the system.

Data acquisition

Data acquisition and control of the filtration test rig was made via a data-logging computer system based on LabVIEW^{TM} (National Instruments): a detailed description of its automation can be found elsewhere [43]. Pressure transducers measured the TMP (PXM419-010BA10V, Omega Engineering) and *dp* (PX419-2.5DWUV, Omega Engineering, accuracy of ± 0.08% best fit straight line). The position of the probe was monitored by a potentiometer (534, VishaySpectrol) and a linear variable differential transformer (LVDT) (SM-series LVDT, Singer Instruments) with an accuracy of ± 0.5 μm. A Coriolis flowmeter (Mini CORI-FLOW, Bronkhorst) measured and controlled the gauging mass flow rate during the FDG measurements. The precision balance (Quintix®3102-1S, Sartorius) monitored the amount of permeate collected.

4.4 Calibration

The thickness of fouling layers formed on the top of a membrane can be estimated from a series of calibration data to determine the relationship between *dp* and the distance of the FDG probe to the membrane surface. During FDG calibration, a solid plate was mounted in the flow cell instead of a membrane. Deionized water was circulated throughout the test section and the nozzle tip of the probe was brought into contact with the metal segment of the plate. The position at which the probe contacted the metal segment was verified by measuring the electrical resistance with a multimeter. At this position, the distance of the probe from the surface was set to zero. The probe was then moved by small increments away from the plate and, at each stop, *dp* was measured. This was repeated until the point when the resistance became infinity, and this position was then set as the reference point.

The calibration curve was generated by logging the *dp* readings at a range of normalized probe distances, h_0/d_t, until *dp* reached 100 mbar. Using the Curve Fitting Toolbox^{TM} in MATLAB, a function was derived from the data values in the incremental zone, $h_0/d_t \leq 0.25$.

In Paper I, the calibration data was taken from earlier work [25,26]. Their master calibration curve equation is given by Eq. 4.1 thus:

$$dp = c_1 exp\left(\frac{c_2}{h/d_t}\right) + c_3 exp\left(\frac{c_4}{h/d_t}\right) \tag{4.1}$$

where $c_1 = 1135$, $c_2 = -1.58$, $c_3 = 2.58$, $c_4 = 0.30$ and $R^2 = 0.99$.

A set of experimental calibration data was recorded in Paper II, operated at the following cross-flow conditions: TMP = 40 kPa, CFV = $\sim$0.07 m s^{-1} and $m_g = 0.1$ g s^{-1}. The master calibration curve equation is given by Eq. 4.2 as:

$$dp = c_1 \left(\frac{h}{d_t}\right)^{c_2} + c_3 \tag{4.2}$$

where $c_1 = 0.098$, $c_2 = -2.267$, $c_3 = 4.703$ and $R^2 = 0.999$.

The exact position of the membrane had to be verified experimentally for each filtration experiment. The *dp* vs. h_0/d_t values from the membrane calibration curve were superimposed onto the master calibration curve by adjusting the measurements with the h_0 offset value, $h_{0,\text{offset}}$, to overlap with the master calibration curve, as shown in Fig. 4.2. The $h_{0,\text{offset}}$ value varies for each experiment and is used to correct for the shift in the position of the membrane.

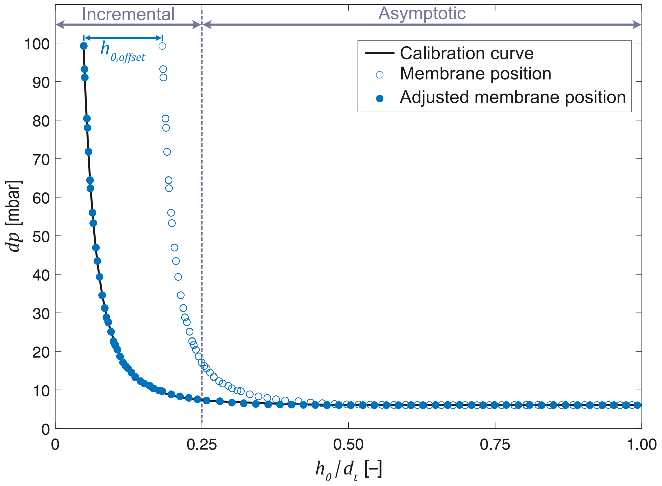

Fig. 4.2. Master calibration curve and an example of experimental data for determining the position of the membrane in which the normalized probe distances, h_0/d_t, were adjusted using the $h_{0,\text{offset}}$ value.

4.5 STEX Liquor Filtration

The PSU membranes were initially swelled and rinsed in deionized water at least a day prior to cross-flow UF. An initial feed STEX liquor volume of ~4 L (pH 3.7, 23–25 °C) was used in all UF experiments. The test rig was operated at the following cross-flow conditions: CFV = $\sim$0.07 m s^{-1} (Re_{duct} = $\sim$1200), TMP = 200 kPa ± 5% and m_g = 0.1 g s^{-1} (pressure-mode FDG).

Pure water flux and membrane position

The pure water flux of the PSU membrane was verified by circulating 5 L of deionized water for at least 1 h. The exact position of the membrane was determined by following the procedures described in Section 4.4 Calibration.

STEX fouling and FDG measurements

After circulating deionized water to determine the pure water flux and membrane position, the feed line was transferred to the feed STEX liquor. Cross-flow UF was performed for at least 2 h, with the FDG probe retracted to the top of the flow cell (i.e. outside the LVDT range) to minimize its disturbance on the formation of the fouling layer, and no gauge flow in order to conserve the STEX liquor. After an initial 30 or 45 min of fouling, FDG measurements were conducted by lowering the probe towards the fouling layer in small increments whilst the system was still subjected to UF of the STEX liquor at a constant gauging mass flow rate of m_g = 0.1 g s^{-1}. FDG measurements were terminated when *dp* reached 100 mbar. The flux curves were not affected during FDG measurements; the imprint of the probe was only $\sim 1 \cdot 10^{-6}$ m^2 in diameter, which is significantly smaller than the active membrane area of $2.4 \cdot 10^{-3}$ m^2 (150 mm × 16 mm).

The probe was retracted to the top of the flow cell after the first FDG measurements. A further 30 or 45 min of fouling allowed foulants to redeposit on top of the membrane and new FDG measurements were conducted thereafter. The STEX fouling and FDG measurement cycle was continued until at least 2 h of UF had elapsed. At the end of each cross-flow UF, the permeate and retentate were collected for characterization. Initial feed STEX samples were also collected prior to cross-flow UF. The test rig was cleaned after each run by washing each section with dishwasher detergent and water; deionized water was also recirculated for 0.5–1.0 h to ensure that the system was cleaned thoroughly.

4.6 MCC Filtration

The cross-flow MF sequence was comprised of four cycles of the following steps: determining the pure water flux and membrane position, MCC fouling, FDG measurements and membrane cleaning and flushing. The cross-flow MF experiments were conducted with an initial MCC suspension volume of 5 L operated at the following conditions: CFV = ~0.07 m s^{-1} (Re_{duct} = ~1200), TMP = 40 kPa ± 5% and $m_g = 0.1$ g s^{-1} (pressure-mode FDG). The fouled PES membrane was collected for scanning electron microscopy (SEM) imaging at the end of each sequence.

Pure water flux and membrane position

The exact position of the PES membrane was determined according to the procedures described in Section 4.4 Calibration. The pure water flux of the membrane was verified by circulating 5 L of deionized water for at least 2000 s (33.3 min).

MCC fouling and FDG measurements

Once deionized water had been circulated, the feed line was diverted to the 0.02 vol% MCC suspension for at least 3000 s (50 min), with the FDG probe retracted to the top of the flow cell and no gauge flow. FDG measurements were conducted by approaching the fouling layer in small increments at a constant gauging mass flow rate of $m_g = 0.1$ g s^{-1} until a *dp* of 100 mbar is reached.

Cleaning and flushing of the membrane

The membrane was inspected visually after the first FDG measurements to investigate the extent of fouling. The fouled PES membrane was cleaned physically by flushing the fouling layer with deionized water and removing it with a soft-bristled paintbrush. Deionized water was also circulated for 1800 s (30 min) to remove the remaining MCC in the test rig.

The cleaned PES membrane was mounted back into the flow cell and a new pure water flux and membrane position were determined by circulating a fresh set of deionized water for at least 2000 s (33.3 min). This was followed by 3000 s (50 min) of additional fouling with a fresh 0.02 vol% MCC suspension, which allowed MCC particles to redeposit on the active membrane surface; FDG measurements were conducted thereafter. The MF sequence was continued until four cycles had been completed.

4.7 Characterization of Membranes and Process Streams

After performing the cross-flow filtration experiments, the different process streams (feed, permeate and retentate) were analyzed (Paper I) and the pristine and fouled PES membranes characterized (Paper II). Representative liquor samples were frozen using liquid nitrogen prior to the membranes and process streams being characterized: the samples taken were freeze-dried using a FreeZone® Triad™ Freeze Dry System.

Laser diffraction

The feed STEX liquor (heated and non-heated) was analyzed for its particle size distribution by laser diffraction (Mastersizer 2000, Malvern Panalytical, detection range of 0.02–2000 μm).

Klason lignin and acid-soluble lignin

The freeze-dried process stream samples were hydrolyzed using 72% sulfuric acid to obtain the Klason lignin or the acid-insoluble residual material after hydrolysis [74]. The hydrolysates were analyzed for their acid-soluble lignin (ASL) concentration using UV absorption at 205 nm (SPECORD®205, Analytik Jena), taking the molar absorptivity constant of 110 L g^{-1} cm^{-1} [75].

High-performance anion-exchange chromatography

The carbohydrate content of the hydrolysates from the Klason lignin analysis was also determined. The monomeric sugars present in the freeze-dried process stream samples after hydrolysis were quantified using a Dionex ICS-5000 HPLC system equipped with CarboPac™ PA1 columns, with NaOH and 0.2 M NaOH/NaAc eluents. This high-performance anion-exchange chromatography system has a pulsed amperometric detector and uses the Chromeleon 7 software (Chromatography Data System, Version 7.1.0.898).

Scanning electron microscopy

The freeze-dried membrane samples were coated with gold for 30 s at 60 mA using a sputter coater (Q150 Plus Series, Quorum Technologies) prior to imaging via SEM. The sputtered samples were visualized using an SEM (JSM-7800FPRIME, JEOL), equipped with an upper secondary electron detector at an acceleration voltage of 5 kV, to obtain their morphological features.

4.8 Molecular Dynamics Simulations

In Paper II, the experimental FDG technique was complemented with computational MD simulations to extract information on the fouling mechanisms at the molecular level [76]. By studying the nano/molecular-scale effects of the foulant-foulant and foulant-membrane interactions at the membrane-solvent interface, an in-depth mechanistic understanding of the membrane fouling behavior can be gained.

The atomic configuration of the MD simulation system is described in detail in Paper II, using an all-atom optimized potentials for liquid simulations (OPLS-AA) as the force field to describe cellulose [77,78] and the PES membrane [79,80]. The cellulose structure was modelled from a starting structure of cellulose crystals consisting of eight anhydroglucose units [81], as shown in Fig. 4.3. Two different types of surfaces were present in the modelled structure, namely 110 and 200, within which the interactions between the 110–110, 110–200 and 200–200 planes were considered [82].

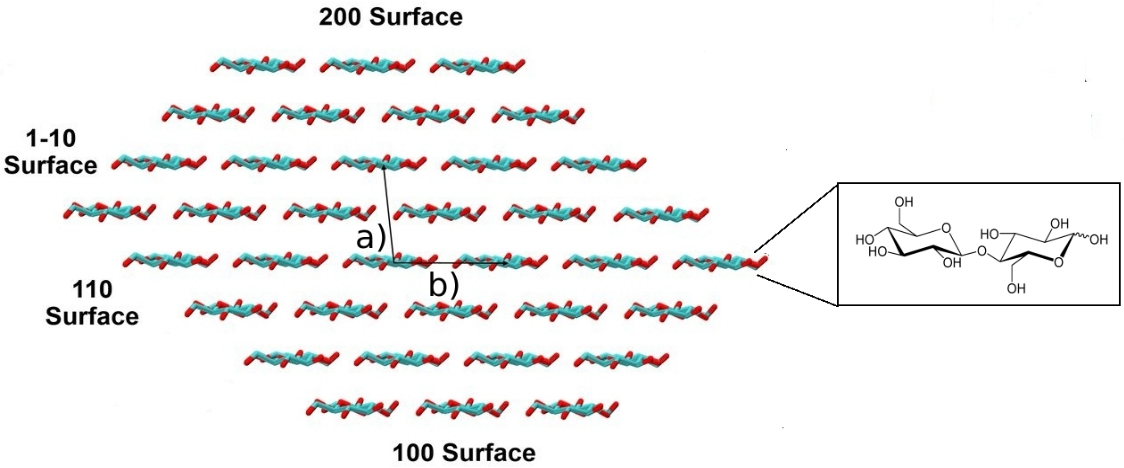

Fig. 4.3. A cellulose crystal, comprised of eight anhydroglucose units, and its respective faces.

Fig. 4.4 shows the PES polymer chain that was modelled by repeating 200 monomer units. The density of the modelled PES polymer was 1.34 g cm^{-3}, which was close to the 1.37 g cm^{-3} experimental value reported by Barth *et al.* [83].

The potential of mean force (PMF) as a function of the interparticle distance (reaction coordinate) was calculated by employing the weighted histogram analysis method (WHAM) [84]. The interactions of the two systems in water, i.e. (1) cellulose-cellulose and (2) cellulose-PES membrane, were determined using umbrella sampling (US) conducted at 300K and 320 K. In the former system, two cellulose crystals were placed in a simulation box of size $5.10 \times 10.36 \times 3.19$ nm^3 at a certain interparticle distance,

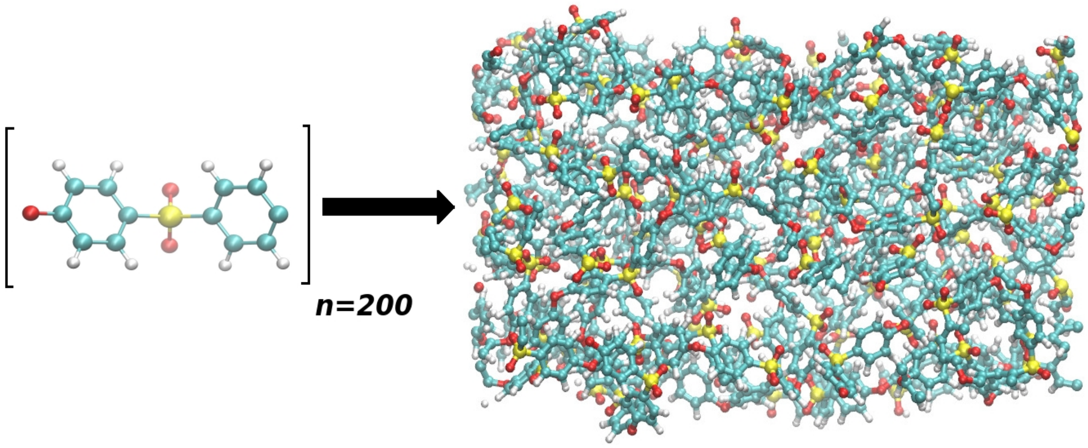

Fig. 4.4. A PES membrane formed by repeating 200 monomer units (shown within brackets).

which was then filled with the required number of water molecules. One crystal was used as a reference while the other was pulled towards it with force constant of 65000 kJ mol^{-1} nm^{-1}. In the latter system, the PES membrane was placed in a computational box of 3.20 × 4.68 × 12.00 nm^3 and a cellulose crystal was placed 2.1 nm from the membrane surface. The box was also then filled with the required number of water molecules and the US was initiated by pulling the cellulose crystal towards the PES membrane at a constant velocity of 0.005 nm ps^{-1} with a force constant of 65000 kJ mol^{-1} nm^{-1}. The configurations in both systems were stored at 0.05 nm intervals and 6 ns sampling time.

Using the US method, the entropy was calculated from ΔG at each interparticle separation, r, taking the finite difference temperature derivative of PMF, with $T = 300$ K and $\Delta T = 20$ K. The entropy is given by Eq. (4.3) [85]:

$$-\Delta S(r) = \frac{\Delta G(r, T + \Delta T) - \Delta G(r, T)}{\Delta T} \tag{4.3}$$

The enthalpic contribution to the free energy, ΔH, was calculated using Eq. (4.4):

$$\Delta H = \Delta G + T\Delta S \tag{4.4}$$

5 | Results and Discussion

5.1 Characterization of Process Streams

The different process streams (feed, permeate and retentate) in Paper I were characterized using various analytical techniques. The particle size distribution, the carbohydrate and lignin content of the feed STEX liquors and the membrane-fractionated samples are presented in the following section.

Particle size distribution

The volume-based size distribution of the particles and agglomerates in the feed STEX liquor is shown in Table 5.1 and Fig. 5.1. The feed STEX liquor was heated under stirring to 40 °C after being stored at 5 °C and three repeated measurements from the same feed STEX liquor were performed. Fig. 5.1 shows that two distinct peaks were detected at $\sim$0.2 μm and $\sim$70 μm, with distributions of 0.5 vol% and 4.4 vol%, respectively. The peak at $\sim$70 μm is also closest to the D_{50} value of 43.1 μm.

Table 5.1. Size distribution of the particles and agglomerates present in the feed STEX liquor.

Sample	**D**$_{10}[\mu m]$	**D**$_{50}[\mu m]$	**D**$_{90}[\mu m]$
STEX liquor*	2.3	43.1	183.8

* heated to 40 °C

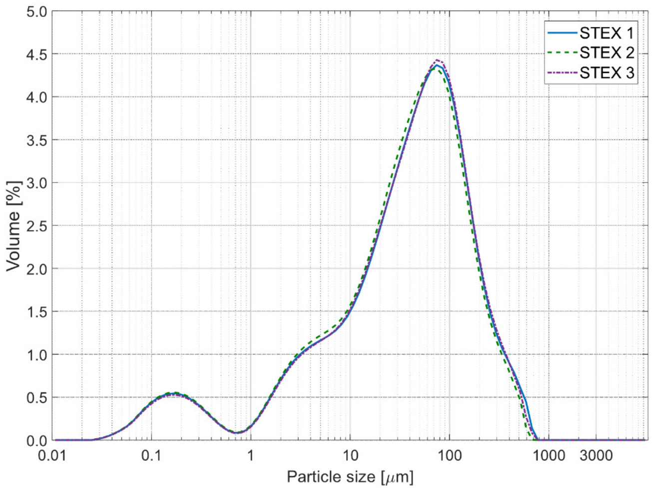

Fig. 5.1. Size distribution of the feed STEX liquor heated to 40 °C [86].

Composition

Table 5.2 reports the carbohydrate and lignin content of the process streams in Paper I, with values given in wt% of the freeze-dried samples. The composition of the feed STEX liquor was similar to that obtained in an earlier work on the membrane fractionation of STEX liquor by Mattsson *et al.* [87]. Their results showed an increase in the arabinose content and a decrease in the mannose content from the feed STEX liquor to the permeate stream, both of which were observed for all runs in this study, too. Arabinose, as a side chain of the hemicellulose xylan, can be cleaved from the backbone making it prone to autohydrolysis, thus forming smaller species that can accumulate on the permeate side. Dissolved extractives [88], fatty acids and other organic compounds [89] may be present both in the feed STEX liquor and the membrane-fractionated samples, and thereby account for the remaining percentage of the composition.

Table 5.2. Composition of anhydrosugar and lignin content in the feed and membrane-fractionated STEX liquor samples in [wt%] [86].

Sample	Run No.	Arabinose	Galactose	Glucose	Xylose	Mannose	Klason lignin	ASL	Total
Feed STEX liquor[a]		8.9	5.4	5.8	6.5	20.0	12.4	2.5	61.5
Feed STEX liquor[b]	1	10.1	6.2	6.5	7.5	23.2	14.7	3.3	71.5
Permeate	1	15.3	5.6	4.2	9.7	15.8	12.0	3.5	66.1
Feed STEX liquor	2	9.4	5.3	6.5	7.3	20.7	13.3	3.5	66.0
Retentate	2	9.0	5.1	6.0	7.2	20.5	13.0	3.2	64.0
Permeate[b]	2	16.5	4.8	3.4	8.0	12.7	10.9	5.8	62.1
Feed STEX liquor	4	8.3	5.7	6.8	8.0	24.5	11.0	3.2	67.5
Retentate	4	8.2	5.6	6.7	7.8	23.5	16.3	3.1	71.2
Permeate	4	10.7	4.9	5.3	9.1	20.5	8.6	4.2	63.3
Retentate	5	8.3	5.5	6.7	7.7	23.5	11.0	2.8	65.5
Permeate	5	11.0	5.3	5.7	8.8	21.3	9.4	4.0	65.5

[a] same sample analyzed for particle size distribution

[b] calculated average of two measurements

5.2 Characterization of Fouled Membranes

Zhou *et al.* [26] made a characterization on the same batch of MCC as used in this work and measured the zeta potential and the surface morphology of the PES membrane by streaming potential measurements and using atomic force microscopy. At pH levels of 5.8 and 5.6, the zeta potential of the PES membrane was -87 ± 0.3 mV and -74 ± 0.5 mV, respectively. The membrane had a root-mean-square surface roughness, R_q, of 328 ± 36 nm, while its arithmetic mean surface roughness, R_a, was 260 ± 35 nm.

The surface topographies of the pristine and fouled PES membranes in Paper II are shown in Fig. 5.2. Comparing the top surface of the pristine and fouled membranes (Figs. 5.2a and c), open pores were observed in the former and partially blocked pores in the latter, despite this membrane being cleaned physically. This blocking of surface pores confirms the formation of cake layers and provides an indication of irreversible fouling (intermediate and/or complete blocking) during cross-flow MF. On the other hand, open pores were observed on the bottom surface of both pristine and fouled membranes (Figs. 5.2b and d), indicating that it is less likely that MCC particles had passed through the membrane, and that pore blocking of the membrane may not have occurred. If some smaller particles entered the pores of the membrane, it seemed that they just passed through, partly due to the weak interaction with the membrane material and partly because the membrane have larger pore sizes on the permeate side (i.e. asymmetric membrane).

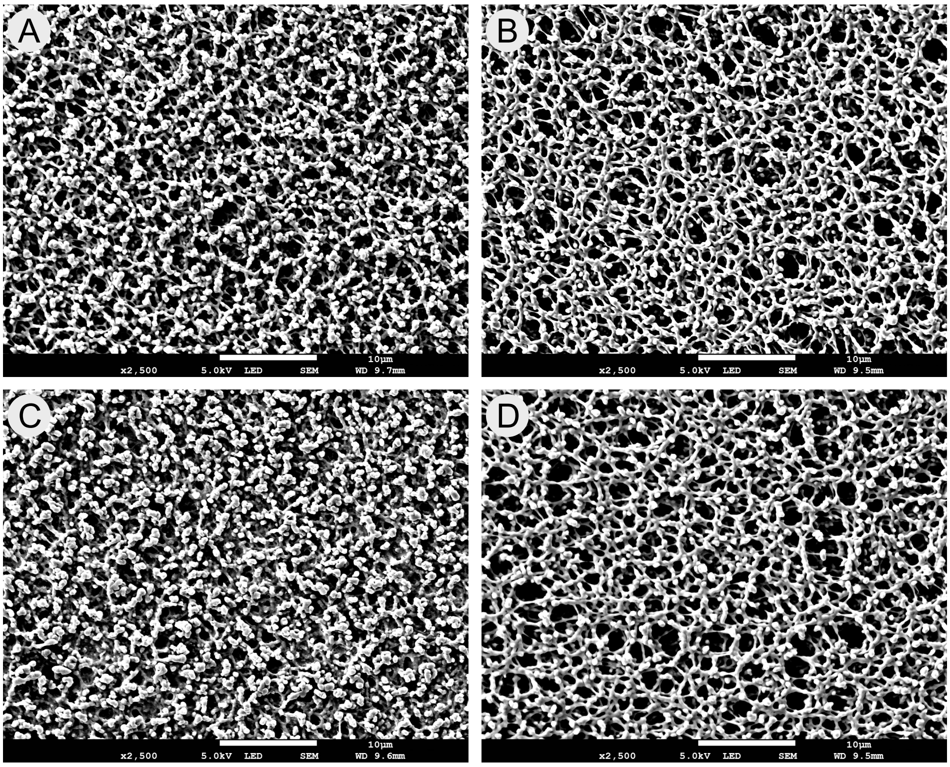

Fig. 5.2. SEM micrographs of the PES membranes at 2500x magnification. Pristine membrane: (A) top and (B) bottom surfaces. Fouled membrane: (C) top and (D) bottom surfaces.

5.3 Flux Profiles

STEX liquor filtration

Cross-flow UF experiments were performed to investigate the fouling behavior of the STEX liquors presented above. The superimposed curves of pure water and permeate flux are shown in Fig. 5.3, with TMP kept constant at 200 kPa ± 5%. A relatively broad range of pure water flux values, from 160 and 360 L m^{-2} h^{-1}, was measured between individual runs (Fig. 5.3a). This variation in flux values is probably due to the amount of residual foulants in the test rig varying between runs. Immediately after changing the feed material from deionized water to STEX liquor, a massive decline in the permeate flux was observed (Fig. 5.3b), with flux values dropping to < 15 L m^{-2} h^{-1} by the time the first FDG measurements were made. This shows that a polarization/cake layer (i.e. fouling layer) with a high flow resistance was formed and/or internal pore fouling occurred very quickly. The flux values declined gradually at the latter part of the UF and, after 120 min of cross-flow UF, the permeate flux values for Runs 2, 3, 4 and 5 were 5.6, 8.0, 7.4 and 5.7 L m^{-2} h^{-1}, respectively. There may be several reasons for this slow decrease in flux (i.e. increase of flow resistance): the slow growth of the polarization/cake layer, the rearrangement of this layer above the membrane and the slow increase of internal fouling.

It should be noted that there were fewer data points for Runs 1 and 3: results from Run 1 were calculated manually with longer time intervals, using a less precise precision balance (PB3002-S, Mettler Toledo). In the case of Run 3, only flux values between 75 and 150 min were considered because the contact of the flow cell permeate tube with the permeate container resulted in unstable weight readings. Despite these limitations, the permeate flux curves for all runs nevertheless showed a consistent trend.

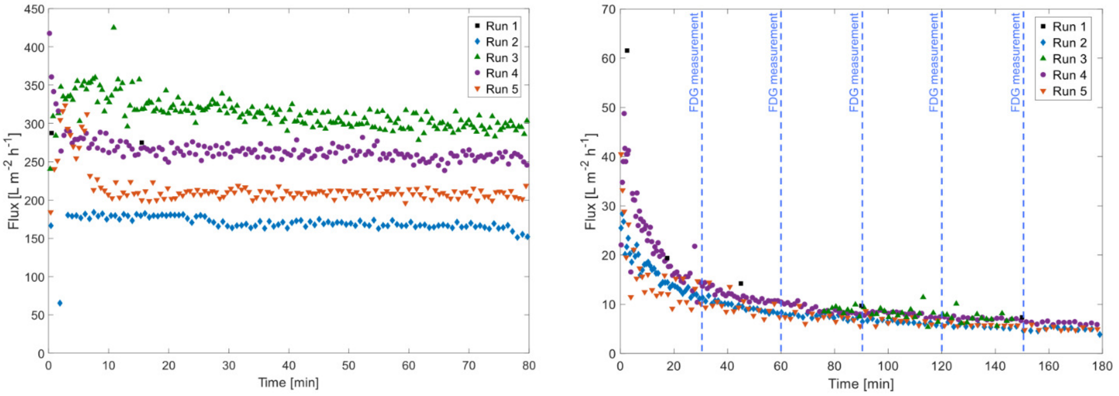

a. Pure water flux at 200 kPa TMP

b. Permeate flux at 200 kPa TMP

Fig. 5.3. Flux curves versus filtration time for Runs 1 to 5 showing (a) the pure water flux and (b) the permeate flux of a PSU membrane during cross-flow UF at 200 kPa TMP. Dashed lines indicate the start of FDG measurements. N.B. Run 1 had time intervals of 45 min [86].

MCC filtration

Fig. 5.4 shows the pure water and permeate flux curves of the pristine, fouled and cleaned PES membranes for each cycle of the cross-flow MF experiments in Paper

II. A gradual decline in the pure water flux of the pristine membrane was observed after circulating deionized water for 2000 s (33.3 min): the flux values decreased from $2.53{\cdot}10^4\ \mathrm{L\,m^{-2}\,h^{-1}}$ to $2.45{\cdot}10^4\ \mathrm{L\,m^{-2}\,h^{-1}}$. When the feed line was diverted from deionized water to MCC suspension, a sharp decline in permeate flux was observed immediately, indicating that the deposition of initial foulants caused a high flow resistance at a constant TMP. After 3000 s (50 min) of MCC fouling, the flux values dropped to around $500\ \mathrm{L\,m^{-2}\,h^{-1}}$ or $\sim$2% of the initial pure water flux of the pristine membrane.

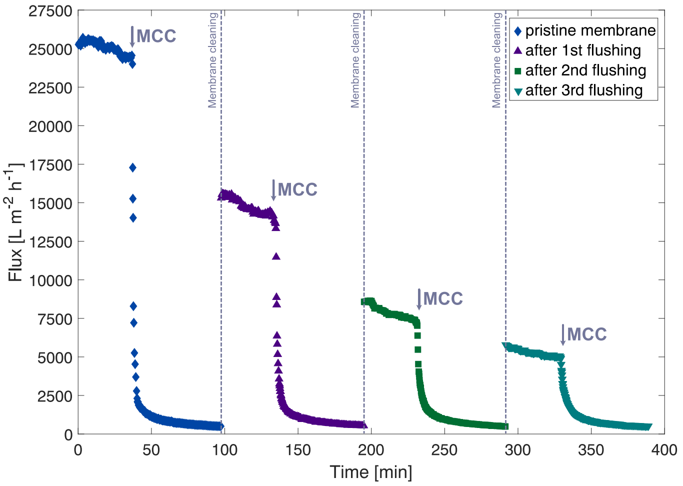

Fig. 5.4. Flux vs. filtration time for the cross-flow MF sequence of MCC suspensions. Dashed lines indicate membrane cleaning and flushing procedure.

The particle size distribution of mechanically-treated MCC suspensions was determined by Lidén *et al.* [16] using laser diffraction. Their results on the same batch of MCC indicate that the nominal pore size of the PES membrane is significantly smaller than almost all MCC particles: this suggests that the formation of a cake layer is the primary fouling mode, as MCC particles were deposited on top of the PES membrane (i.e. MCC particles were retained on the feed side). However, this does not exclude the internal blocking of pores since smaller particles may pass through larger pores, as the sizes indicated were all nominal. But, as mentioned above, no signs of internal pore blocking could be detected when the membranes was characterized.

A successive reduction in the pure water flux was observed after each membrane was subjected to the cleaning and flushing procedure, as seen in Fig. 5.4. Despite the thoroughness in the cleaning procedures, an increase in flow resistance after each MF cycle suggests the presence of irreversible fouling, hindering the flow of liquid due to MCC particles being bound strongly to the membrane (at least partly intermediate and/or complete blocking as described above). It is nevertheless interesting to note that, despite the large differences in the pure water flux, the trend of the permeate flux decline was not only consistent but also did not appear to have been influenced by the initial flux or the fact that the membrane was partially fouled.

The pure water flux declined gradually while deionized water was circulated throughout the test rig in both the STEX liquor (Paper I) and MCC suspension (Paper II) studies. This gradual decline may indicate the presence of residual foulants from earlier experiments, as Zhou and Mattsson [25] observed for dilute MCC suspensions. However, the differences in the initial pure water flux had a minimal influence on the permeate flux decline during cross-flow filtration, reaching similar flux values by the end of filtration in both the UF and MF studies.

Based on the permeate flux curves, severe fouling of the PSU and PES membranes may have occurred in different modes (e.g. cake formation, polarization layer and/or pore blockage) [15]. These fouling modes may occur simultaneously, so further investigation is therefore necessary to build an in-depth understanding of the contribution of each mechanism.

5.4 FDG Profiles

STEX liquor filtration

The *dp* vs. h/d_t profiles obtained during cross-flow UF of STEX liquors at 200 kPa TMP are presented in Fig. 5.5. The FDG measurements made with deionized water for determining the membrane position of a pristine membrane without any fouling layer, shown as filled black squares (■), followed a consistent trend: a baseline *dp* in the asymptotic zone ($h/d_t >$ 0.25) and a sharp increase in *dp* in the incremental zone ($h_0/d_t \leq$ 0.25) as the probe approaches the membrane.

An increase in *dp* further away from the pristine membrane corresponds to a thicker fouling layer. The thickness of a fouling layer is the difference in h/d_t values of the pristine membrane and the measurements made after 30 or 45 min of fouling (including measurements after 30 or 45 min of additional fouling). Although the thickest fouling layers were observed after the first measurements, as seen in all five profiles, they became continually thinner after a series of additional fouling and measurements. One possible reason for this response is that the build-up of fouling layers was faster initially due to higher permeate flow at the start of cross-flow UF, as seen in the flux curves in Fig. 5.3. After the first measurements had been made, some of the deposited

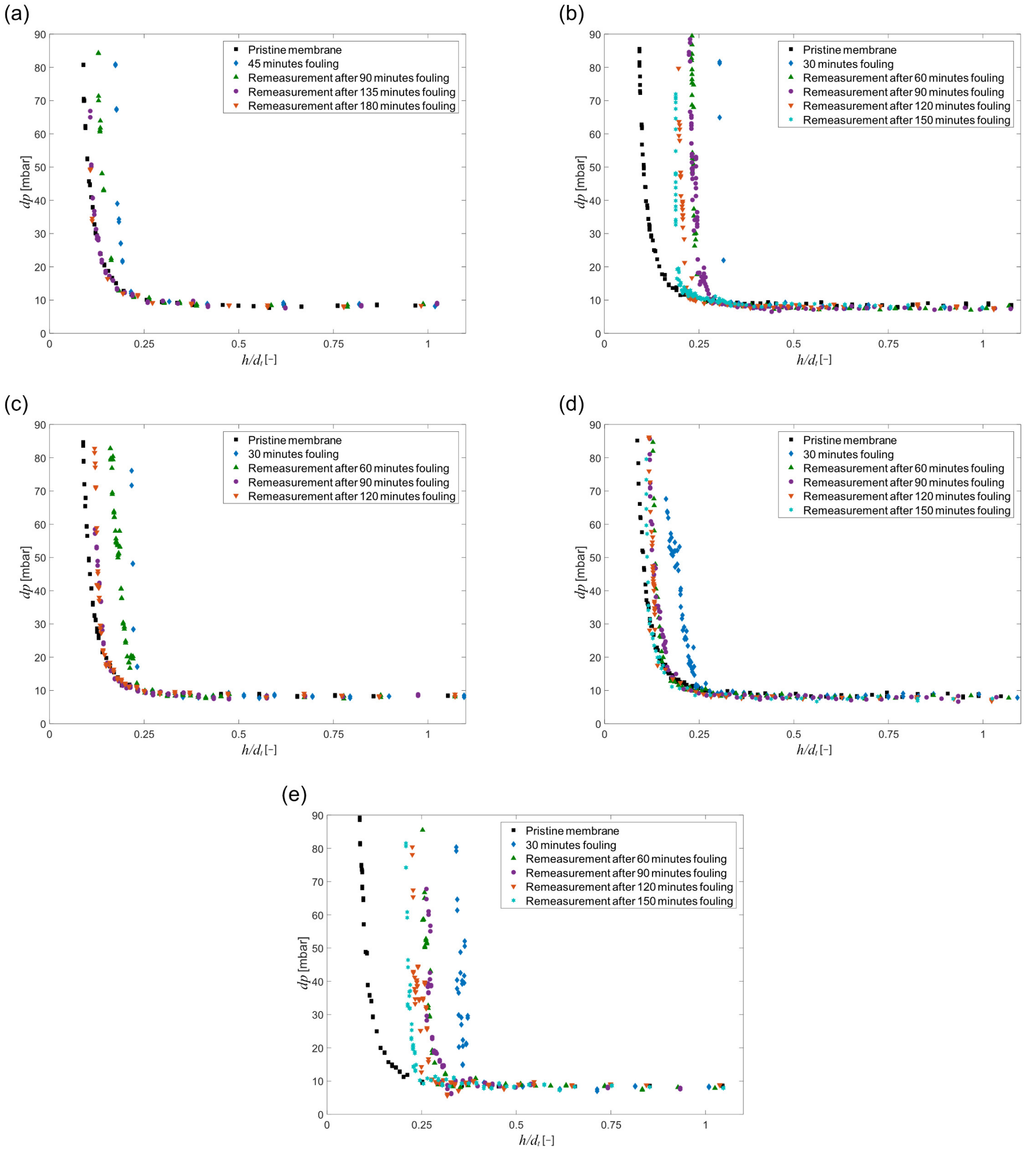

Fig. 5.5. FDG profiles showing the differential pressure, dp, and the normalized probe distances, h/d_t, during cross-flow UF of STEX liquors at 200 kPa TMP. (a) Run 1, (b) Run 2, (c) Run 3, (d) Run 4 and (e) Run 5. N.B. The x-axis for the pristine membrane curve (■) is h_0/d_t due to the absence of a fouling layer [86].

materials were sheared off. However, no new additional deposition was observed at lower permeate flows because stronger shear forces hindered the build-up of fouling layers at the same impact area of the FDG probe. Consequently, the decrease in the thickness of the fouling layer is maybe caused either by a smaller tendency of materials to accumulate at the membrane surface after a massive drop in permeate flux or the rearrangement of particles/molecules in the layer.

The later FDG measurements in Runs 1, 3 and 4 (Fig. 5.5a, c and d) almost resembled the pristine membrane curve, with only slight differences at higher *dp* values. The sharper increase of the response may have been caused by the entrapment of particles between the tip of the FDG probe and the fouling layer/membrane surface, which is supported by an increasing *dp* value even at a constant probe position ($< 100\,\mu$m). When foulants were dislodged from underneath the probe tip, a sudden drop in *dp* was observed, which made it difficult to determine the actual thickness of the fouling layers and hindered the estimation of their strength properties.

All of the fouling measurements made in Runs 2 (Fig. 5.5b) and 5 (Fig. 5.5e) were shifted to the right, indicating that the PSU membrane might have moved above its known position during STEX liquor UF. One probable cause of this shift is when a surge in TMP was observed whilst the feed material was being changed from deionized water to STEX liquor. This was rectified in Paper II by modifying the filtration test rig to maintain a constant TMP throughout the entire cross-flow filtration operation.

MCC filtration

The thickness and strength properties of MCC fouling layers during cross-flow MF at 40 kPa TMP were determined using the FDG probe as it approached the surface of the fouling layer. The *dp* vs. h/d_t profiles during the cross-flow MF sequence are shown in Fig. 5.6. The response during FDG measurements on a pristine membrane without any fouling layer, shown by filled black circles (●), were similar to those obtained in the UF case presented above, with a baseline *dp* in the asymptotic zone ($h/d_t >$ 0.25) and a sharp increase in *dp* in the incremental zone ($h_0/d_t \leq$ 0.25).

The thickness of the fouling layer is calculated from the difference in h/d_t values of the pristine membrane and the 3000 s (50 min) MCC fouling (with and without flushing), where a larger difference in h/d_t translates to a thicker fouling layer. From the MCC fouling curves, the initial FDG measurements resembled the pristine membrane up until h/d_t = 1.50 but, as the probe was moved closer to the fouling layer, a gradual increase in *dp* was observed. At h/d_t = 1.20–1.50, the increase in flow resistance is may be the result of an increased concentration of MCC particles exactly above the membrane (i.e. concentration polarization), leading to increased viscosity of the suspension. Below h/d_t = 1.20, the formation of a cake layer is the primary reason for the increased flow resistance. A much sharper increase in *dp* values was observed at $h/d_t <$ 0.50, but the values did not converge with the pristine membrane measurements. This non-convergence demonstrates the resilience of cake layers formed close to the surface of the PES membrane.

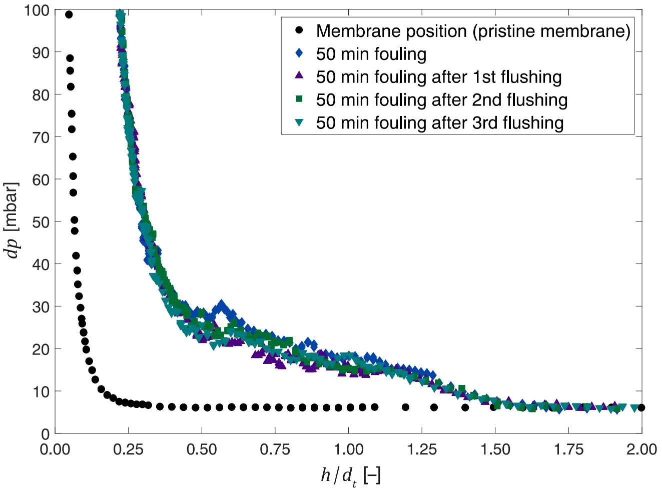

Fig. 5.6. FDG profiles showing the differential pressure, *dp*, and the normalized probe distances, h/d_t, during cross-flow MF of the MCC suspension at 40 kPa TMP. N.B. The curves for the membrane position after each cleaning and flushing of the PES membrane were excluded.

The FDG profiles after each fouling and cleaning cycle revealed cake fouling layers of similar thicknesses. This similarity in response, despite the large variation in initial pure water flux, may indicate that the increased resistance of the membrane did not affect the formation of the cake layer virtually. The sum of the membrane and cake resistance (total resistance), R_{m+c}, can be calculated using Darcy's Law, shown in Eq. 5.1:

$$R_{m+c} = \frac{\text{TMP}}{J\mu} \tag{5.1}$$

where J is the flux and μ is the dynamic viscosity of the fluid.

Fig. 5.7 shows the total resistance, R_{m+c}, plotted against filtration time. A massive surge in R_{m+c} was observed during MCC fouling, with resistance values reaching beyond $3{\cdot}10^8$ m^2 L^{-1}. After each cycle of membrane cleaning and flushing, R_{m+c} increased gradually whilst deionized water was being circulated: this suggests the presence of irreversible fouling as MCC particles are retained and accumulate on the feed side of the PES membrane (cf. membrane characterization above).

Fig. 5.8 illustrates the effect that the applied fluid shear from the gauging fluid flow has on the thickness of the cake layers after each MCC fouling cycle. The maximum fluid shear stress, $\tau_{w,max}$, was calculated using Eq. (3.2). The fouling layer thickness

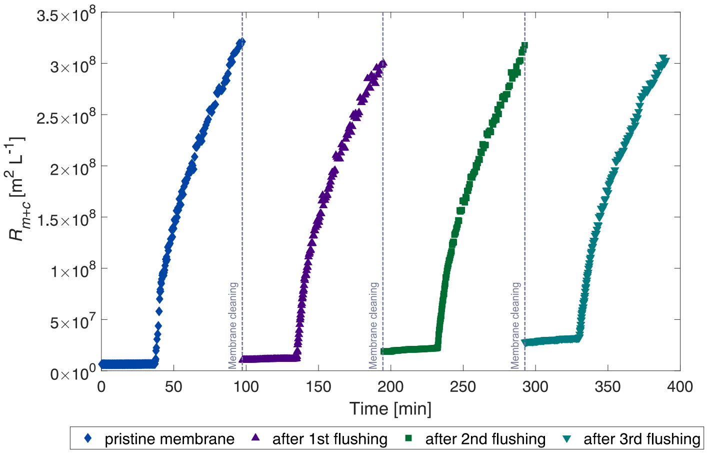

Fig. 5.7. Total resistance, R_{m+c}, over filtration time during cross-flow MF of MCC suspension.

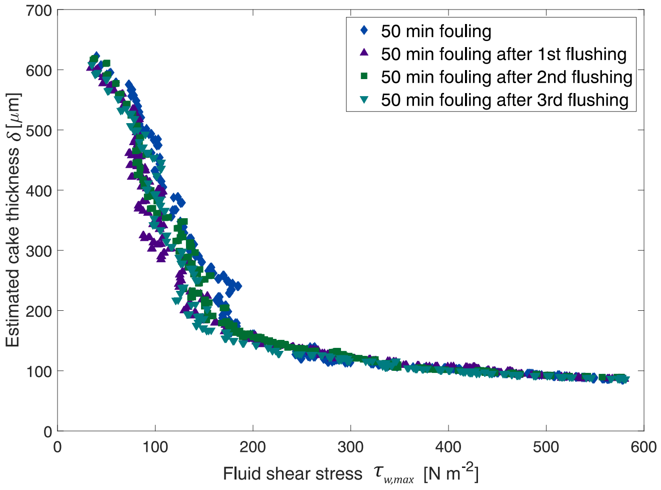

Fig. 5.8. Estimated cake thickness, δ, vs. applied fluid shear, $\tau_{w,max}$, exerted by the FDG probe on the cake layers formed.

after 3000 s (50 min) of MF was estimated as being 616 ± 5 μm at an applied shear stress of 37 ± 2 Pa for both the fouled and re-fouled membranes. In the region of $\tau_{w,max}$ between 35–150 N m^{-2}, loose cake layers were easily sheared off and a reduction in the thickness of the cake from ∼600 μm to 200 μm was recorded; when a minimum of 200 N m^{-2} was applied, thin cake layers of considerably high strength were observed. At the maximum applied shear stress of 580 N m^{-2}, ∼85 μm of the cake layers were difficult to remove: this corresponds to 4–5 nominal sizes or agglomerate diameters of MCC particles. Higher fluid shear was required to remove very resilient cake layers formed closer to the PES membrane (i.e. the cohesive strength of cake layers increases when they are formed closer from the membrane). This effect may be due to the higher local solid pressure exerted on the MCC particles deposited closer to the membrane surface [32].

5.5 Simulation Results

The flux and FDG profiles obtained from the cross-flow MF experiments of MCC suspensions presented above indicated the presence of irreversible fouling that accumulated in each membrane cleaning cycle. Moreover, the cohesive strength of the cake layers formed increases in the direction towards the membrane. With these experimental results, the membrane fouling behavior was investigated further through MD simulations of cellulose-cellulose and cellulose-PES interactions in water at the interface.

Potential of mean force

The PMF profiles of the interactions between the 110–110, 110–200 and 200–200 surfaces, normalized by the final contact area, are shown in Fig. 5.9. The cellulose-cellulose interaction is repulsive in all cases and, when the interacting surfaces become closer, a significant increase in repulsion is observed. However, the presence of an attractive energy region near the crystal interfaces promotes agglomeration of the interacting crystals due to attractive forces at low center of mass (COM) distances. The agglomerates tend to remain closer to the restrained interfaces [90], which is a possible explanation of the formation of highly resilient cake layers close to the membrane, as observed during the cross-flow MF experiments described above.

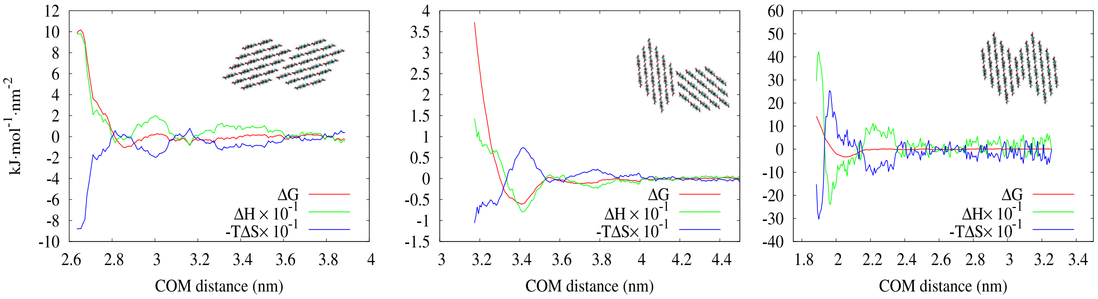

a. 110-110 surface

b. 110-200 surface

c. 200-200 surface

Fig. 5.9. Cellulose–cellulose interactions, showing the enthalpic, ΔH, and entropic, $-T\Delta S$, contributions to the free energy, ΔG, during the interaction of different faces of cellulose crystals.

The PMF profiles of the interactions of the PES membrane with cellulose (100) and (200) surfaces are shown in Fig. 5.10. The cellulose-PES interactions are more repulsive than cellulose-cellulose interactions, confirming that cellulose crystals have a lesser tendency to approach the PES surface. In concordance with cellulose-cellulose interactions, however, attractive energy regions exist at low COM distances, which

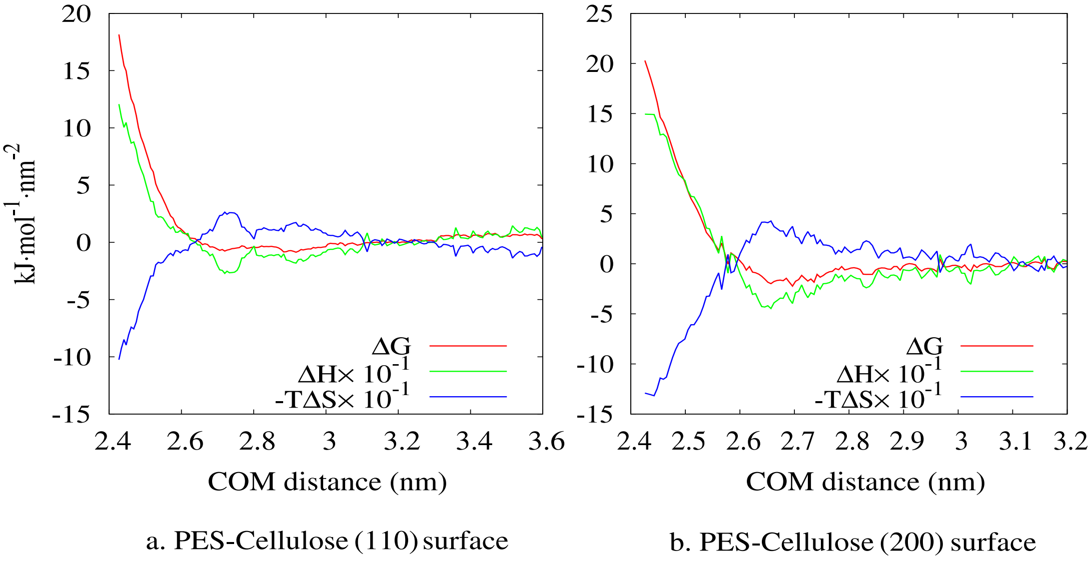

Fig. 5.10. PES-cellulose interaction, showing the free energy, ΔG, profile along with the associated enthalpic, ΔH, and entropic, $-T\Delta S$, contributions for the interaction of the membrane surface and the different faces of cellulose crystals.

suggests that cellulose crystals have a tendency to remain in regions close to the PES membrane. The pressure forces due to the cross-flow also drive the particles towards the interface, making the particles susceptible to remain in the attractive energy regions. Both cellulose (100) and (200) surfaces showed attraction to the PES membrane, which is partially hydrophobic with a water contact angle of ~67 ° [91].

Enthalpic and entropic contributions to the free energy profile

The enthalpic contribution, ΔH, and entropic contribution, $-T\Delta S$, to the PMF, ΔG, wer calculated at 300 K and are shown in using Eqs. 4.3 and 4.4, and are shown in Figs. 5.9 and 5.10. In both figures, the enthalpic and entropic contributions act oppositely; they depend on the interparticle distances and the interacting surface of the cellulose crystals.

In the interaction between the 110–110 and 200–200 surfaces (Fig. 5.9a and c), an energy barrier exists at 2.9–3.1 nm and 2.2–2.4 nm COM distances for 110–110 and 200–200 surfaces, respectively, resulting in an increase in entropy that might be due to the expulsion of interfacial water molecules. When similar surfaces interact, there is a higher probability that similar solvent molecule groups become exposed towards each interacting surface, thereby explaining the similar responses recorded during the interaction of 110–110 and 200–200 surfaces. This is not the case for the interaction of

110–200 surfaces (Fig. 5.9b): their association is limited by a lower primary minimum contributed by lowered entropy. The overall free energy of association, as suggested by the primary minimum, is the least for this case and indicates that the agglomeration of 110 and 200 surfaces is less probable than in other cases. The free energy profiles presented in this study followed a similar trend as that reported by Garg *et al.* [92].

During cross-flow filtration, the TMP pushes dispersed particles towards the membrane from the bulk fluid, affecting the interaction of interfacial particles with the membrane and thereby forming a pronounced fouling layer. The interactions of cellulose surfaces with the PES membrane are shown in Fig. 5.10, where the free energy profiles of 110–PES and 200–PES surfaces were estimated. In both cases, the entropy of the system decreases until the contact minimum is reached, where enthalpy is favorable in that region. Beyond the contact minimum, the entropy increases drastically and becomes favorable for the interaction of the cellulose surface with the PES membrane surface. Thus, cellulose particles tend to remain in the region of the first energy minimum as they approach the PES membrane under the influence of external pressure forces, with the result that they foul the membrane.

The results obtained of the enthalpic and entropic contributions made to the free energy profiles suggest that the interaction of cellulose particles at the contact minimum (i.e. stable state of the system) is exothermic. Increasing the temperature or decreasing the entropy of the system by lowering the Re_{duct} can negatively affect the existence of cellulose crystals at the first energy minimum and reduce the strength of the fouling layers formed [25].

6 | Conclusions

Fluid dynamic gauging (FDG), an *in situ* and real-time technique for monitoring the development of fouling layers, provided data of the thickness and strength of the fouling layers formed on flat sheet membranes. This work confirms that FDG can be employed in characterizing the fouling of membrane by wood components, which can be of particular interest when membrane separation processes are employed in future lignocellulosic biorefineries.

FDG measurements made during cross-flow filtration of steam explosion (STEX) liquors and microcrystalline cellulose (MCC) suspensions revealed information of the build-up rates of fouling layers and their cohesive strength when shear forces were applied. In the method development study for STEX liquor fouling, the FDG profiles obtained during the fouling experiments showed that an initial thick fouling layer with a high resistance was formed rapidly. Although the resistance increased further after this initial phase, it was only gradual, which may be due to pore blocking and/or rearrangement of the structure of the fouling layer. These results also indicate that the highest resistance of the fouling layer is close to the membrane. This method, which has been developed for cross-flow filtration of STEX liquors, is suitable for investigating the fouling behavior of complex, heterogeneous systems.

In the MCC fouling experiments, resilient cake layers of considerably high strength were observed close to the surface of the PES membrane. The molecular dynamics (MD) simulations offered a possible explanation for this: since it was found that if two crystalline cellulose surfaces come very close to each other, there will be attractive forces between these two surfaces and a resilient cake layer will therefore be formed closest to the membrane. This was also true for the cellulose-PES interactions, which is a possible explanation for the irreversible fouling that occurred in the experiments. It demonstrates that experimental cross-flow filtration with FDG measurements, complemented with computational MD simulations, can provide a deeper mechanistic understanding of the fouling phenomena that occur during membrane filtration.

7 | Future Perspectives

Several interesting aspects pertaining to the cross-flow membrane filtration of wood components are worth investigating. Much work can still be undertaken to develop FDG for monitoring the development of fouling layers. It would be of interest to perform MF as a pre-filtration step prior to the UF of STEX liquors, for example, to investigate whether severe fouling is also observed and if particles continue to hinder estimation of the thickness and strength of fouling layers. Moreover, since STEX liquor is a heterogeneous feed containing different wood components, advanced chemical characterization of the membrane-fractionated streams as well as the particles present in the feed are of interest in future investigations. Performing MD simulations of foulant-foulant and foulant-membrane interactions would also provide a better mechanistic understanding of the fouling behavior of STEX liquors.

The process conditions (e.g. CFV, TMP, temperature and ionic strength) during cross-flow filtration can be investigated to identify their effects on the fouling behavior: a lower CFV (i.e. lower Re_{duct}), for example, could aid in reducing the strength of the fouling layers formed [25]. This could be beneficial in uncovering the optimal conditions and improving the cleaning procedures necessary during membrane operations.

Advanced characterizations, such as scattering-based techniques, atomic force microscopy, focused ion beam scanning electron microscopy and rheological analysis of fouled membranes, can be explored to provide new insights into the interactions between the membrane and the fouling layers formed by streams containing wood components.

8 | Acknowledgements

The financial support received from The Knut and Alice Wallenberg Foundation, through the Wallenberg Wood Science Center (WWSC), is gratefully acknowledged.

I would like express my gratitude to the following people, without whom this thesis would not have been possible:

- Associate Professor Tuve Mattsson, my previous main supervisor, for introducing me to the world of membrane filtration. How I wish Chalmers could provide us with the opportunity to continue with this project!
- Professor Hans Theliander, my current main supervisor and examiner, for his excellent guidance, invaluable feedback and words of wisdom that have inspired me to move forward despite the many adversities I faced.
- Professor Anette Larsson, my co-supervisor, for her unwavering support and compassion, and our meaningful scientific and non-scientific discussions.
- Ms. Roujin Ghaffari, for being my go-to colleague when I needed advice and for reassuring me that things will be just fine.
- Dr. Nabin Kumar Karna, for our harmonious collaboration and interesting discussions on molecular dynamics simulations.
- Mr. Anders Ahlbom, for sharing his expertise on size-exclusion chromatography and for making our office such a pleasant work station.
- Ms. Maureen Sondell for providing excellent linguistic reviews of this thesis and its appended papers.
- WWSC Chalmers doctoral students and my colleagues at the Division of Chemical Engineering (Forest Products and Chemical Engineering) for creating a friendly and warm working environment.
- Last, but not least, my parents, siblings and friends for their unconditional support and for being my source of inspiration throughout this journey. *Salamat!*

9 | References

[1] Ragauskas, A.J., Williams, C.K., Davison, B.H., Britovsek, G., Cairney, J., Eckert, C.A., Frederick, W.J., Hallett, J.P., Leak, D.J., Liotta, C.L., Mielenz, J.R., Murphy, R., Templer, R. & Tschaplinski, T. (2006). The path forward for biofuels and biomaterials. *Science*, 311 (5760), 484–489.

[2] Lipnizki, F., Thuvander, J. & Rudolph, G. (2019). Membrane processes and applications for biorefineries. In A. Figoli , Y. Li, & A. Basile (Eds.), *Current Trends and Future Developments on (Bio-) Membranes: Membranes in Environmental Applications* (Vol. 1, pp. 283-301). Elsevier.

[3] Abels, C., Carstensen, F. & Wessling, M. (2013). Membrane processes in biorefinery applications. *Journal of Membrane Science*, 444, 285–317.

[4] Hajilary, N., Rezakazemi, M. & Shirazian, S. (2019). Biofuel types and membrane separation. *Environmental Chemistry Letters*, 17, 1-18.

[5] Huang, H.-J., Ramaswamy, S., Tschirner, U.W. & Ramarao, B.V. (2008). A review of separation technologies in current and future biorefineries, *Separation and Purification Technology*, 62, 1–21.

[6] He, Y., Bagley, D.M., Leung, K.T., Liss, S.N. & Liao, B.-Q. (2012). Recent advances in membrane technologies for biorefining and bioenergy production, *Biotechnology Advances*, 30, 817-858.

[7] Kamali, M. & Khodaparast, Z. (2015). Review on recent developments on pulp and paper mill wastewater treatment, *Ecotoxicology and Environmental Safety*, 114, 326–342.

[8] Yogarathinam, L.T., Ismail, A.F., Goh, P.S. & Gangasalam, A. (2020). Challenges of membrane technology in biorefineries, *Journal of Applied Membrane Science & Technology*, 24, 75–82.

[9] Koros, W.J., Ma, Y.H. & Shimidzu, T. (1996). Terminology for membranes and membrane processes (IUPAC Recommendation 1996), *Journal of Membrane Science*, 120, 149-159.

[10] Uragami, T.(2017). *Science and Technology of Separation Membranes*. John Wiley & Sons, Inc.

[11] Mulder, M. (1996). *Basic Principles of Membrane Technology*. Kluwer Academic Publishers.

[12] Cui, Z., Jiang, Y. & Field, R.W. (2010). Chapter 1 - Fundamentals of pressure-driven membrane separation processes. In Cui & Muralidhara (Eds.) *Membrane Technology* (pp. 1-18). Elsevier Ltd.

[13] Belfort, G., Davis, R.H. & Zydney, A.L. (1994). The behavior of suspensions and macromolecular solutions in crossflow microfiltration. *Journal of Membrane Science*, 96, 1-58.

[14] Suki, A., Fane, A.G. & Fell, C.J.D. (1984). Flux decline in protein ultrafiltration. *Journal of Membrane Science*, 21, 269-283.

[15] Hermia, J. (1982). Constant pressure filtration laws – application to power law non-Newtonian fluids. *Transactions of the Institution of Chemical Engineers*, 60, 183–187.

[16] Lidén, A., Karna, N.K., Mattsson, T. & Theliander, H. (2021). Dewatering microcrystalline cellulose: the influence of ionic strength, *Separation and Purification Technology*, 264, 118245.

[17] Vela, M.C.V., Blanco, S.Á., García, J.L. & Rodríguez, E.B. (2008). Analysis of membrane pore blocking models applied to the ultrafiltration of PEG. *Separation and Purification Technology*, 62, 489–498.

[18] Field, R.W., Wu, D., Howell, J.A.& Gupta, B.B. (1995). Critical flux concept for microfiltration fouling. *Journal of Membrane Science*, 100, 259-272.

[19] Arnal, J.M., García-Fayos, B. & Sancho, M. (2011). Membrane cleaning. *Expanding Issues in Desalination*, 3, 63-84.

[20] Li, H. & Chen, V. (2010). Chapter 10 - Membrane fouling and cleaning in food and bioprocessing. In Cui & Muralidhara (Eds.) *Membrane Technology* (pp. 213-254). Elsevier Ltd.

[21] Maartens, A., Swart, P. & Jacobs, E.P. (1996). An enzymatic approach to the cleaning of ultrafiltration membranes fouled in abattoir effluent. *Journal of Membrane Science*, 119, 9–16.

[22] Sjöström, E. (1993). *Wood Chemistry Fundamentals and Applications* (2nd ed.). Academic Press, San Diego, CA, USA.

[23] Mattsson, T., Sedin, M. & Theliander, H. (2012a). Filtration properties and skin formation of micro-crystalline cellulose. *Separation and Purification Technology*, 96, 139–146.

[24] Mattsson, T., Sedin, M. & Theliander, H. (2012b). On the local filtration properties of microcrystalline cellulose during dead-end filtration. *Chemical Engineering Science*, 72, 51-60.

[25] Zhou, M. & Mattsson, T. (2019). Effect of crossflow regime on the deposit and cohesive strength of membrane surface fouling layers. *Food and Bioproducts Processing*, 115, 185–193.

[26] Zhou, M., Sandström, H., Belioka, M.P., Pettersson, T. & Mattsson, T. (2019). Investigation of the cohesive strength of membrane fouling layers formed during cross-flow microfiltration: The effects of pH adjustment on the properties and fouling characteristics of microcrystalline cellulose. *Chemical Engineering Research and Design*, 149, 52–64.

[27] Sixta, H. (2006). *Handbook of Pulp*. WILEY-VCH Verlag GmbH & Co.KGaA, Weinheim, Germany.

[28] Persson, T. & Jönsson, A.-S. (2010). Isolation of hemicelluloses by ultrafiltration of thermomechanical pulp mill process water – influence of operating conditions. *Chemical Engineering Research and Design*, 88, 1548–1554.

[29] Thuvander, J. & Jönsson, A.-S. (2016). Extraction of galactoglucomannan from thermomechanical pulp mill process water by microfiltration and ultrafiltration -

Influence of microfiltration membrane pore size on ultrafiltration performance. *Chemical Engineering Research and Design*, 105, 171–176.

[30] Al-Rudainy, B., Galbe, M. & Wallberg, O. (2020). From lab-scale to on-site pilot trials for the recovery of hemicellulose by ultrafiltration: experimental and theoretical evaluations. *Separation and Purification Technology*, 250, 117187.

[31] Arkell, A., Krawczyk, H. & Jönsson, A.-S. (2013). Influence of heat pretreatment on ultrafiltration of a solution containing hemicelluloses extracted from wheat bran.*Separation and Purification Technology*, 119, 46–50.

[32] Mattsson, T., Lewis, W.J.T., Chew, Y.M.J. & Bird, M.R. (2015). In situ investigation of soft cake fouling layers using fluid dynamic gauging. *Food and Bioproducts Processing*, 93, 205–210.

[33] Mattsson, T., Lewis, W.J.T., Chew, Y.M.J. & Bird, M.R. (2018). The use of fluid dynamic gauging in investigating the thickness and cohesive strength of cake fouling layers formed during cross-flow microfiltration. *Separation and Purification Technology*, 198, 25–30.

[34] Marselina, Y., Le-Clech, P., Stuetz, R. & Chen, V. (2008). Detailed characterisation of fouling deposition and removal on a hollow fibre membrane by direct observation technique. *Desalination*, 231, 3–11.

[35] Schluep, T. & Widmer, F. (1996). Initial transient effects during cross flow microfiltration of yeast suspensions. *Journal of Membrane Science*, 115, 133–145.

[36] Kromkamp, J., Faber, F., Schroen, K. & Boom, R. (2006). Effects of particle size segregation on crossflow microfiltration performance: control mechanism for concentration polarisation and particle fractionation. *Journal of Membrane Science*, 268, 189–197.

[37] Mairal, A.P., Greenberg, A.R., Krantz, W.B. & Bond, L.J., 1999. Real-time measurement of inorganic fouling of RO desalination membranes using ultrasonic time-domain reflectometry. *Journal of Membrane Science*, 159, 185–196.

[38] Yao, S., Costello, M., Fane, A.G. & Pope, J.M. (1995). Non-invasive observation of flow profiles and polarisation layers in hollow fibre membrane filtration modules using NMR micro-imaging. *Journal of Membrane Science*, 99, 207–216.

[39] David, C., Pignon, F., Narayanan, T., Sztucki, M., Gésan-Guiziou, G. & Magnin, A. (2008). Spatial and temporal in situ evolution of the concentration profile during casein micelle ultrafiltration probed by small-angle x-ray scattering. *Langmuir*, 24, 4523–4529.

[40] Coster, H.G.L., Chilcott, T.C. & Coster, A.C.F., (1996). Impedance spectroscopy of interfaces, membranes and ultrastructures, *Bioelectrochemistry and Bioenergetic*, 40, 79–98.

[41] Tuladhar, T.R., Paterson, W.R., Macleod, N. & Wilson, D.I. (2000). Development of a novel non-contact proximity gauge for thickness measurement of soft deposits and its application in fouling studies. *The Canadian Journal of Chemical Engineering*, 78, 935–947.

[42] Rudolph, G., Virtanen, T., Ferrando, M., Güell, C., Lipnizki, F. & Kallioinen, M. (2019). A review of in situ real-time monitoring techniques for membrane fouling in the biotechnology, biorefinery and food sectors. *Journal of Membrane Science*, 588, 117221.

[43] Lewis W.J.T. (2015). *Advanced Studies of Membrane Fouling: Investigation of Cake Fouling Using Fluid Dynamic Gauging* [Ph.D. thesis, University of Bath].

[44] Chew, Y.M.J., Paterson, W.R. & Wilson, D.I. (2007). Fluid dynamic gauging: a new tool to study deposition on porous surfaces. *Journal of Membrane Science*, 296, 29-41.

[45] Lewis, W.J.T., Mattsson, T., Chew, Y.M.J. & Bird, M.R. (2017). Investigation of cake fouling and pore blocking phenomena using fluid dynamic gauging and critical flux models. *Journal of Membrane Science*, 533, 38–47.

[46] Lewis, W.J.T., Chew, Y.M.J. & Bird, M.R. (2012). The application of fluid dynamic gauging in characterising cake deposition during the cross-flow microfiltration of a yeast suspension. *Journal of Membrane Science*, 405–406, 113-122.

[47] Chew, J.Y.M., Cardoso, S.S.S., Paterson W.R. & Wilson, D.I. (2004a). CFD studies of dynamic gauging. *Chemical Engineering Science*, 59. 3381-3398.

[48] Chew, J.Y.M., Paterson, W.R., & Wilson, D.I. (2004b). Fluid dynamic gauging for measuring the strength of soft deposits. *Journal of Food Engineering*, 65. 175-187.

[49] Chew, J.Y.M., Tonneijk, S.J., Paterson, W.R. & Wilson, D.I.(2006). Solvent-based cleaning of emulsion polymerization reactors. *Chemical Engineering Journal*, 117, 61-69.

[50] Peck, O.P.W., Bird, M.R., Bolhuis, A. & Chew, Y.M.J. (2015). Application of Fluid Dynamic Gauging in the Characterization and Removal of Biofouling Deposits. *Heat Transfer Engineering*, 36, 685-694,

[51] Gordon, P.W., Brooker, A.D.M., Chew, Y.M.J., Wilson, D.I. & York, D.W. (2010). Studies into the swelling of gelatine films using a scanning fluid dynamic gauge. *Food and Bioproducts Processing*, 88, 357-364.

[52] Gordon, P.W., Brooker, A.D.M., Chew, Y.M.J., Letzelter, N., York, D.W. & Wilson, D.I. (2012). Elucidating enzyme-based cleaning of protein soils (gelatine and egg yolk) using a scanning fluid dynamic gauge. *Chemical Engineering Research and Design*, 90, 162-171.

[53] Yang, Q., Ali, A., Shi, L. & Wilson, D.I. (2014). Zero discharge fluid dynamic gauging for studying the thickness of soft solid layers. *Journal of Food Engineering*, 127, 24-33.

[54] Peralta, J.M., Chew, Y.M.J. & Wilson, D.I. (2011a). An analytical method for selecting the optimal nozzle external geometry for fluid dynamic gauging. *Chemical Engineering Science*, 66, 3579-3591.

[55] Peralta, J.M., Chew, Y.M.J. & Wilson, D.I. (2011b). Effect of nozzle external geometry on the pressure and shear stress exerted on the surface being gauged in fluid dynamic gauging. *Chemical Engineering Research and Design*, 89, 2540-2551.

[56] Tuladhar, T.R., Paterson, W.R. & Wilson, D.I. (2002a). Investigation of alkaline cleaning-in place of whey protein deposits using dynamic gauging. *Food and Bioproducts Processing*, 80, 199-214.

[57] Tuladhar, T.R., Paterson, W.R. & Wilson, D.I. (2002b). Thermal conductivity of whey protein films undergoing swelling: measurement by dynamic gauging. *Food and Bioproducts Processing*, 80, 332-339.

[58] Chew, J.Y.M., Paterson, W.R., Wilson, D.I., Höufling, V. & Augustin, W. (2005). A method for measuring the strength of scale deposits on heat transfer surfaces. *Developments in Chemical Engineering and Mineral Processing*, 13, 21-30.

[59] Hooper, R.J., Paterson, W.R. & Wilson, D.I. (2006). Comparison of whey protein model foulants for studying cleaning of milk fouling deposits. *Food and Bioproducts Processing*, 84, 329-337.

[60] Gu, T., Chew, Y.M.J., Paterson, W.R. & Wilson, D.I. (2009a). Experimental and CFD studies of fluid dynamic gauging in duct flows. *Chemical Engineering Science*, 64, 219-227.

[61] Gu, T., Chew, Y.M.J., Paterson, W.R. & Wilson, D.I. (2009b). Experimental and CFD studies of fluid dynamic gauging in annular flows. *AIChE Journal*, 55, 1937-1947.

[62] Gu, T., Albert, F., Augustin, W., Chew, Y.M.J., Paterson, W.R., Scholl, S., Sheikh, I., Wang, K. & Wilson, D.I. (2011). Fluid dynamic gauging applied to annular test apparatuses for fouling and cleaning. *Heat Transfer Engineering*, 32, 339-348.

[63] Jones, S.A., Chew, Y.M.J., Bird, M.R. & Wilson, D.I. (2010). The application of fluid dynamic gauging in the investigation of synthetic membrane fouling phenomena. *Food and Bioproducts Processing*, 88, 409-418.

[64] Jones, S.A., Chew, Y.M.J., Wilson, D.I. & Bird, M.R. (2012). Fluid dynamic gauging of microfiltration membranes fouled with sugar beet molasses. *Journal of Food Engineering*, 108, 22-29.

[65] Lister, V.Y., Lucas, C., Gordon, P.W., Chew, Y.M.J. & Wilson, D.I. (2011). Pressure mode fluid dynamic gauging for studying cake build-up in cross-flow microfiltration. *Journal of Membrane Science*, 366, 304-313.

[66] Lewis, W.J.T., Chew, Y.M.J. & Bird, M.R. (2012). The application of fluid dynamic gauging in characterising cake deposition during the cross-flow microfiltration of a yeast suspension. *Journal of Membrane Science*, 405–406, 113-122.

[67] Jørgensen, M.K. & Mattsson. T. (2021). Quantifying charge effects on fouling layer strength and (ir)removability during cross-flow microfiltration. *Membranes* 11, 28.

[68] Tsai, J.-H., Cuckston, G.L., Hallmark, B. & Wilson, D.I. (2019). Fluid-dynamic gauging for studying the initial swelling of soft solid layers. *AIChE Journal*, 65, e16664.

[69] Tsai, J.-H., Cuckston, G.L., Schnöing, L., Augustin, W., Scholl, S., Hallmark, B. & Wilson, D.I. (2021). Fluid dynamic gauging for studying early stages of swelling of fouling deposits. *Heat Transfer Engineering*, 1-11.

[70] Tsai, J.-H., Hallmark, B. & Wilson, D. I. (2019b). Integrated fluid dynamic gauge for measuring the thickness of soft solid layers immersed in opaque, viscous, and/or non-Newtonian liquids in situ. *Industrial & Engineering Chemistry Research*, 58, 23124-23134.

[71] Jedvert, K., Saltberg, A. & Theliander, H. (2013). Mild steam explosion followed by kraft cooking and oxygen delignification of spruce (picea abies). *Appita Journal: Journal of the Technical Association of the Australian and New Zealand Pulp and Paper Industry*, 66(4):322.

[72] Jedvert, K., Saltberg, A., Lindström, M., & Theliander, H. (2012). Mild steam explosion and chemical pre-treatment of Norway spruce. *Bioresources*, 7, 2051–2074.

[73] Wetterling, J., Mattsson, T. & Theliander, Hans. (2014). Effects of surface structure on the filtration properties of microcrystalline cellulose. *Separation and Purification Technology*, 136. 1–9.

[74] Theander, O. & Westerlund, E.A. (1986). Studies on dietary fiber. 3. Improved procedures for analysis of dietary fiber. *Journal of Agricultural and Food Chemistry*, 34, 330–336.

[75] Lin, S. & Dence, C. (1992). *Methods in lignin chemistry*. Springer Series in Wood Science.

[76] Ma, Y., Velioğlu, S. Yin, Z., Wang, R. & Chew, J.W. (2021). Molecular dynamics investigation of membrane fouling in organic solvents. *Journal of Membrane Science*, 632, 119329.

[77] Paajanen, A., Sonavane, Y., Ignasiak, D., Ketoja, J.A., Maloney, T. & Paavilainen, S. (2016). Atomistic molecular dynamics simulations on the interaction of TEMPO-oxidized cellulose nanofibrils in water, *Cellulose*, 23, 3449–3462.

[78] Paajanen, A., Ceccherini, S. Maloney,T. & Ketoja, J.A. (2019). Chirality and bound water in the hierarchical cellulose structure. *Cellulose*, 26, 5877–5892.

[79] Roberts, B.P., Krippner, G.Y., Scanlon, M.J. & Chalmers, D.K. (2009). Molecular dynamics of variegated polyamide dendrimers. *Macromolecules*, 42, 2784-2794.

[80] Bisoi, S., Mandal, A.K., Padmanabhan, V. & Banerjee, S. (2017). Aromatic polyamides containing trityl substituted triphenylamine: gas transport properties and molecular dynamics simulations, *Journal of Membrane Science*, 522, 77-90.

[81] Nishiyama, Y., Langan, P. & Chanzy, H. (2002). Crystal structure and hydrogen-bonding system in cellulose Iβ from synchrotron x-ray and neutron fiber diffraction. *Journal of the American Chemical Society*, 124, 9074–9082.

[82] Mehandzhiyski, A.Y., Rolland, N., Garg, M., Wohlert, J., Linares, M. & Zozoulenko, I. (2020). A novel supra coarse-grained model for cellulose. *Cellulose*, 27, 4221–4234.

[83] Barth, C. & Wolf, B.A. (2000). Quick and reliable routes to phase diagrams for polyethersulfone and polysulfone membrane formation, *Macromolecular Chemistry and Physics*, 201, 365–374.

[84] Kumar, S., Rosenberg, J.M., Bouzida, D., Swendsen, R.H. & Kollman, P.A. (1995). Multidimensional free-energy calculations using the weighted histogram analysis method. *Journal of Computational Chemistry*, 16, 1339-1350.

[85] Choudhury, N. & Pettitt, B.M. (2006). Enthalpy-entropy contributions to the potential of mean force of nanoscopic hydrophobic solutes, *The Journal of Physical Chemistry B*, 110, 8459-8463.

[86] Arandia, K., Balyan, U. & Mattsson, T. (2021). Development of a fluid dynamic gauging method for the characterization of fouling behavior during cross-flow filtration of a wood extraction liquor. *Food and Bioproducts Processing*, 128, 30-40.

[87] Mattsson, T., Azhar, S., Eriksson, S., Helander, M., Henriksson, G., Jedvert, K., Lawoko, M., Lindström, M., McKee, L., Oinonen, P., Westerberg, N. & Theliander, H. (2017). The development of a wood-based materials-biorefinery. *Bioresources*, 12, 9152–9182.

[88] Wojtasz-Mucha, J., Mattsson, C., Hasani, M. & Theliander, H. (2019). Pretreatment and cooking of forest residues. *Bioresources*, 14, 9454–9471.

[89] Jedvert, K., Hasani, M., Wells, Jr., T. & Theliander, H. (2014). Analyses of wood components in mild steam explosion liquors from spruce. *Nordic Pulp & Paper Research Journal*, 29, 557–566.

[90] Saha, S., Hemraz, U.D. & Boluk, Y. The effects of high pressure and high temperature in semidilute aqueous cellulose nanocrystal suspensions. *Biomacromolecules*, 21, 1031-1035.

[91] Fu, W., Carbrello, C., Wu, X. & Zhang, W. (2017). Visualizing and quantifying the nanoscale hydrophobicity and chemical distribution of surface modified polyethersulfone (PES) membranes. *Nanoscale*, 9, 15550-15557.

[92] Garg, M., Linares, M. & Zozoulenko, I. (2020). Theoretical rationalization of self-assembly of cellulose nanocrystals: effect of surface modifications and counterions. *Biomacromolecules*, 21, 3069-3080.